Supplementary Information (SI) for Energy & Environmental Science.

Supporting Information

Local phase-modulated heterostructures for perovskite solar cells with high-efficiency and ultra-stability

Yongjoon Cho[1,5], Donghwan Koo[3], Hak-Won Nho[4], Jeewon Park[1], Sangjin Yang[1], Ye-Jin Kim[4], Seonghun Jeong[1], Zhe Sun[1], Gyujeong Jeong[3], Eunbin Son[3], Oh-Hoon Kwon[4], Hyesung Park[6,7]*, Changduk Yang[1,2]**

[1]School of Energy and Chemical Engineering, Perovtronics Research Center, Low Dimensional Carbon Materials Center, Ulsan National Institute of Science and Technology (UNIST), 50 UNIST-gil, Ulju-gun, Ulsan 44919, South Korea

[2]Graduate School of Carbon Neutrality, Ulsan National Institute of Science and Technology (UNIST), 50 UNIST-gil, Ulju-gun, Ulsan 44919, South Korea

[3]Department of Materials Science and Engineering, Graduate School of Semiconductor Materials and Devices Engineering, Graduate School of Carbon Neutrality, Low Dimensional Carbon Materials Center, Ulsan National Institute of Science and Technology, Ulsan, 44919, South Korea

[4]Department of Chemistry, Ulsan National Institute of Science and Technology (UNIST), Ulsan 44919, South Korea

[5]Department of Chemistry and Materials Research Center, Northwestern University, 2145 Sheridan Road, Evanston, IL 60208, USA

[6]KU-KIST Graduate School of Converging Science and Technology, Korea University, 145 Anam-ro, Seongbuk-gu, Seoul 02841, South Korea

[7]Department of Integrative Energy Engineering, Korea University, 145 Anam-ro, Seongbuk-gu, Seoul 02841, South Korea

*e-mail: yang@unist.ac.kr, hyesungpark@korea.ac.kr, ohkwon@unist.ac.kr

Experimental Section

Materials

All starting materials and reagents for synthesizing CY were purchased from Sigma-Aldrich, Alfa Aesar Chemical Company, and Tokyo Chemical Industry Co., Ltd. and used without any further purification. All solvents were ACS and anhydrous grade by distillation. The following materials were used for fabricating PSCs: formamidinium iodide (>99%), lead iodide (>99%), methylammonium chloride (>99%), titanium diisopropoxide bis(acetylacetonate), and Spiro-OMeTAD and purchased from Lumtec, GreatCell Solar, Tokyo Chemical Industry.

Material synthesis

Synthesis of 12,13-bis(2-ethylhexyl)-3,9-diundecyl-12,13-dihydro-[1,2,5]thiadiazolo[3,4-e]thieno[2",3":4',5']thieno[2',3':4,5]pyrrolo[3,2-g]thieno[2',3':4,5]thieno[3,2-b]indole (1). **1** was synthesized according to the reported method[1].

Synthesis of 12,13-bis(2-ethylhexyl)-2-(trimethylstannyl)-3,9-diundecyl-12,13-dihydro-[1,2,5]thiadiazolo[3,4-e]thieno[2",3":4',5']thieno[2',3':4,5]pyrrolo[3,2-g]thieno[2',3':4,5]thieno[3,2-b]indole (2). In a flask, compound **1** (0.4 g, 0.41 mmol) was dissolved in tetrahydrofuran (40 ml), then cooled to -78 °C. Lithium diisopropylamide (2 M in hexane, 0.21 ml) was added slowly to the solution of compound **1** under argon protection. After stirring for 1 hour, trimethyltin chloride (0.12 g, 0.60 mmol) was added and stirred for 6 hours at room temperature. The reaction mixture was quenched, extracted with diethyl ether, and dried over magnesium sulfate. The brown liquid was obtained (0.45 g, 97%) and used for the next step without further purification.

Synthesis of 7-(12,13-bis(2-ethylhexyl)-3,9-diundecyl-12,13-dihydro-[1,2,5]thiadiazolo[3,4-e]thieno[2",3":4',5']thieno[2',3':4,5]pyrrolo[3,2-g]thieno[2',3':4,5]thieno[3,2-b]indol-2-yl)benzo[c][1,2,5]thiadiazole-4-carbaldehyde (**3**). In a flask, compound **2** (0.4 g, 0.35 mmol), 7-bromobenzo[*c*][1,2,5]thiadiazole-4-carbaldehyde (0.1 g, 0.42 mmol), and tetrakis(triphenylphosphine)palladium(0) (0.02 g, 0.018 mmol) were dissolved in toluene (30 ml). The mixture was stirred at 100 °C overnight under argon protection. After cooling to room temperature, the solvent was removed under reduced pressure. The residue was purified by column chromatography with hexane and dichloromethane to afford the red solid (0.35 g, 84%). ^{1}H NMR ($CDCl_3$, 400 MHz) δ ppm 10.82 (s, 1H), 8.35 (d, J = 7.4 Hz, 1H), 7.91 (d, J = 7.4 Hz, 1H), 7.04 (s, 1H), 4.64 (m, 4H), 2.99 (m, 2H), 2.83 (t, J = 7.7 Hz, 2H), 2.05 (m, 2H), 2.01 – 1.82 (m, 4H), 1.31 – 0.88 (m, 54H), 0.66 – 0.58 (m, 12H).

Synthesis of (Z)-5-((7-(12,13-bis(2-ethylhexyl)-3,9-diundecyl-12,13-dihydro-[1,2,5]thiadiazolo[3,4-e]thieno[2'',3'':4',5']thieno[2',3':4,5]pyrrolo[3,2-g]thieno[2',3':4,5]thieno[3,2-b]indol-2-yl)benzo[c][1,2,5]thiadiazol-4-yl)methylene)-3-ethyl-2-thioxothiazolidin-4-one (**4**). In a flask, compound **3** (0.30 g, 0.27 mmol) and 3-ethylrhodanine (0.21 g, 1.32 mmol) were dissolved in chloroform (20 ml), then piperidine (0.20 ml) was added. The mixture was stirred at 80 °C overnight under argon protection. After cooling to room temperature, the mixture was poured into methanol and filtered. The residue was purified by column chromatography with hexane and dichloromethane, yielding a purple solid (0.30 g, 89%). ^{1}H NMR ($CDCl_3$, 400 MHz) δ ppm 8.57 (s, 1H), 7.85 (d, J = 7.6 Hz, 1H), 7.81 (d, J = 7.6 Hz, 1H), 4.62 (m, 4H), 4.27 (q, J = 7.2 Hz, 2H), 2.99 (m, 2H), 2.84 (m, 2H), 2.06 (m, 2H), 1.96 – 1.85 (m, 4H), 1.45 – 0.82 (m, 57H), 0.69 – 0.57 (m, 12H).

Synthesis of (Z)-10-(7-((3-ethyl-4-oxo-2-thioxothiazolidin-5-ylidene)methyl)benzo[c][1,2,5]thiadiazol-4-yl)-12,13-bis(2-ethylhexyl)-3,9-diundecyl-12,13-dihydro-[1,2,5]thiadiazolo[3,4-e]thieno[2'',3'':4',5']thieno[2',3':4,5]pyrrolo[3,2-g]thieno[2',3':4,5]thieno[3,2-b]indole-2-carbaldehyde (**5**). In a flask, anhydrous dimethylformamide (1.05 mL), phosphorus oxychloride (1.3 mL), and 1,2-dichloroethane (2.0 mL) were added at 0 °C, and the mixture was stirred for 30 min. Then, the mixture was transferred dropwise to the solution of compound **4** (0.30 g, 0.24 mmol) in 1,2-dichloroethane (10 mL) and stirred at 130 °C overnight. The reaction mixture was quenched with $NaHCO_3$, extracted with dichloromethane, and dried over magnesium sulfate. The residue was purified by column chromatography with hexane and dichloromethane to afford the dark purple solid (0.25 g, 83%). ^{1}H NMR ($CDCl_3$, 400 MHz) δ ppm 10.14 (s, 1H), 8.79 (s, 1H), 7.86 (s, 2H), 4.65 (m, 4H), 3.90 (q, J = 7.1 Hz, 2H), 3.21 (t, J = 7.7 Hz, 2H), 2.98 (m, 2H), 2.09 – 1.90 (m, 6H), 1.52 – 0.83 (m, 57H), 0.71 – 0.56 (m, 12H).

Synthesis of CY (**6**). In a flask, compound **5** (0.25 g, 0.19 mmol) and 2F-IC (0.13 g, 0.57 mmol) were dissolved in chloroform (30 ml), then pyridine (1 ml) was added. The mixture was stirred at 80 °C overnight under argon protection. After cooling to room temperature, the mixture was poured into methanol and filtered. The residue was purified by column chromatography with hexane and chloroform, yielding a blue solid (0.26 g, 90%). ^{1}H NMR ($CDCl_3$, 400 MHz) δ ppm 9.13 (s, 1H), 8.79 (s, 1H), 8.54 (m, 1H), 7.86 (m, 2H), 7.68 (t, J = 7.5 Hz, 1H), 4.71 (m, 4H), 3.90 (q, J = 7.2 Hz, 2H), 3.22 (t, J = 7.8 Hz, 2H), 2.98 (m, 2H), 2.10 (m, 2H), 1.90 (m, 4H), 1.53 – 0.83 (m, 57H), 0.75 – 0.59 (m, 12H). ^{13}C NMR ($CDCl_3$, 100 MHz) δ ppm 167.21, 165.87, 154.42, 154.23, 153.60, 147.81, 147.47, 144.72, 144.56, 138.38, 136.79, 136.72, 136.53, 135.54, 135.23, 132.79, 130.47, 129.79, 129.59, 129.27, 126.39, 124.80, 124.30, 123.48, 119.08, 115.20, 114.82, 114.05, 111.75, 67.86, 55.56, 55.26, 40.31, 40.15, 37.41, 31.94, 31.27, 29.87, 29.78, 29.67, 29.65, 29.58, 29.54, 29.48, 29.38, 29.03, 27.04, 23.31, 23.28, 23.15, 23.09, 22.84, 22.83, 22.72, 14.15, 13.78, 13.20, 10.16, 10.08. Elemental analysis: anal. calcd C, 64.13; H, 6.05; N, 8.31; S, 16.91. Found: C, 64.11; H, 6.04; N, 8.29; S, 16.93. HRMS (ESI) m/z 1515.5031 ($C_{81}H_{91}F_2N_9O_2S_8$ calcd. for m/z 1515.5029).

Structural characterization and DFT calculation

^{1}H nuclear magnetic resonance (NMR) and ^{13}C NMR spectra of the materials were recorded on a Bruker AVANCE III HD 400 MHz spectrometer using deuterated $CDCl_3$ as solvent and tetramethylsilane (TMS) as an internal standard, and ^{1}H NMR spectra of the films were recorded on VNMRS 600 MHz (Agilent, USA) spectrometer using DMF-d_7 as solvent. Elemental analysis was investigated using a Flash EA 2000 series at the Korea Basic Science Institute. High resolution mass spectrometry (HRMS) spectra were measured using AccuTOF 4G+ DART. DFT calculations were performed using the Gaussian 09 package at B3LYP function and the 6-31G+** basis set.

Device fabrication

PSCs were fabricated in n-i-p structure with a configuration of fluorine-doped tin oxide on glass (FTO)/TiO_2/perovskite/Spiro-OMeTAD/Au. The FTO electrode was cleaned with deionized water, acetone, and IPA by sonication, followed by O_2 plasma treatment for 5 min. The planar TiO_2 layer was deposit by spin-coating process with titanium diisopropoxide bis(acetylacetonate)/ethanol (1:10, *v*/*v*) solution. On top of the planar TiO_2 layer, a mesoporous TiO_2 layer was deposited by spin-coating a TiO_2 paste dispersion (ethanol/terpineol (78:22, *v*/*v*)). Then annealed at 500 °C on a hot plate for 1 h in ambient air to crystallize TiO_2. After, perovskite precursor solution (1.8 M of formamidinium lead iodide powder and 30 mol% of methylammonium chloride) dissolved in a 4:1 (*v*/*v*) mixture of DMF and DMSO) was spin-coated on mesoporous TiO_2 layer at 6,000 rpm for 50 s. During the spin-coating process, CB (including CY) was dropped onto the perovskite film at a predefined time point, followed by annealing at 150 and 100^{o}C for 10 and 30 min, respectively. The spin-coating process was carried out inside a clean hood under strictly regulated environmental conditions, with the relative humidity maintained between 15–20% RH and the temperature controlled between 20–25^{o}C. Then, Spiro-OMeTAD with an ionic dopant (FK-209, dissolved in acetonitrile with optimized concentration) and 4-tert-butylpyridine was deposited by the spin-coating (4,000 rpm for 30 s). Finally, the Au electrode was thermally evaporated to a thickness of 100 nm under a base pressure of 2×10^{-6} Torr. The device efficiency was measured in a N_2-filled glove box at room temperature. The p-i-n structured PSCs were fabricated with a configuration of ITO/PTAA/perovskite/$PC_{61}BM$/ZnO nanoparticles/Ag. The ITO-coated glass substrate was cleaned using a detergent, deionized water, acetone, and isopropanol (IPA). All substrates were treated with O_2 plasma. The PTAA (2 mg mL^{-1} in CB) was deposited on the ITO substrate by spin-coating at 4,000 rpm for 60 s. Then, the perovskite film was deposited on the ITO/PTAA substrate. For the electron transport layer, $PC_{61}BM$ (20 mg mL^{-1} in CB) and ZnO nanoparticles (dissolved in isopropyl alcohol) were sequentially deposited on the perovskite layer by spin-coating at 3,000 rpm for 30 s and 4,000 rpm for 60 s, respectively. Finally, the patterned 100-nm thick Ag was thermally evaporated for the top electrode. All fabrication steps for both control and CY-containing devices were kept strictly identical, with the sole difference being the presence or absence of CY in the anti-solvent.

J–V and EQE measurements

J–V curves were measured using a Xenon lamp solar simulator with a Keithley 2635A source meter under standard test conditions (AM 1.5G, 100 mW cm^{-2}). The active area of devices was 0.08 and 1.0 cm^2 for small- and large-area device, respectively. The calibration was conducted with a standard silicon reference cell. Light-intensity dependent J_{sc} and V_{oc} were measured using neutral density filters. The value of α was obtained from the power law described as $J_{sc} \propto I^{\alpha}$ under short-circuit conditions. The slope of V_{oc} varies were calculated via following relation, $V_{oc} \propto (kT/q)\ln I$ under open circuit conditions. EQE measurements were carried out for the PSCs using a QEX7 system (Model QEX7, PV Measurements).

Energy level measurement

UPS measurements were performed with an ultraviolet He I lamp (21.2 eV, ESCALAB 250XI, Thermo Fisher Scientific). The UPS spectra were collected at 2 eV pass energy with 3 V bias voltage. CV measurement was performed on an Iviumstat.h with a three-electrode cell system in a nitrogen bubbled 0.1 M tetra-*n*-butylammonium hexafluorophosphate (n-Bu_4NPF_6) solution in acetonitrile at a scan rate of 100 mV^{-1} s^{-1} at room temperature. An Ag/Ag$^+$ electrode, platinum wire, and material-coated glassy carbon electrode were used as the reference electrode, counter electrode, and working electrode, respectively.

SEM measurement

SEM images of perovskite films (top-view and cross-sectional view) including EDX elemental mapping were analyzed with Cold Fe-SEM microscope (S-4800, Hitachi).

In situ PL measurement

In situ PL measurements were recorded using a dynamic spectrometer (DU-300, Shaanxi Puguangweishi Technology, China) under 650 nm laser excitation. The PL spectra were collected during thermal annealing at 100oC under ambient conditions (40–50% RH).

ToF-SIMS measurement

The uniformly distributed CY molecules were examined by a ToF-SIMS system (ToF-SIMS 5, ION ToF) with pulsed primary ions from Cs^+ (1 keV) liquid–metal ion gun for sputtering and Bi^+ (25 keV) pulsed primary ion beam for detecting negative ions for analysis.

XRD and GIWAXS measurements

XRD analyses were conducted with the D8 DISCOVERY (Bruker) diffractometer using Cu-Kα radiation (at wavelength of 1.5418 Å). GIWAXS measurements were conducted at the PLS-II 9A beamline of the Pohang Accelerator Laboratory in Korea. The X-rays coming from the in-vacuum undulator were monochromated ($\lambda = 1.10994$ Å) using a double crystal monochromator and focused both horizontally and vertically (450 (H) × 60 (V) μm^2 in FWHM (full width at half maximum) @ the sample position) using K–B type mirrors. The GIXD sample stage was equipped with a 7-axis motorized stage for the fine alignment of the sample, and the incidence angle of the X-ray beam was set to be 0.3°. The GIXD patterns were recorded with a 2D CCD detector (Rayonix SX165) and the X-ray irradiation time was 5–30 s, dependent on the saturation level of the detector. Diffraction angles were calibrated using a sucrose standard (monoclinic, P21, $a = 10.8631$ Å, $b = 8.7044$ Å, $c = 7.7624$ Å, and $\beta = 102.938°$) and the sample-to-detector distance was ≈231 mm.

GIXRD measurement

GIXRD analysis was conducted with a D8 DISCOVERY (Bruker) diffractometer using Cu Kα radiation (at a wavelength of 1.5418 Å) by varying the incident angles.

High-resolution TEM measurement

The detailed morphologies of the perovskite films were characterized using high resolution TEM (JEM-2100F, JEOL) at an accelerating voltage of 200 kV.

XPS and FT-IR measurements

XPS of Pb 4f for perovskite was investigated using monochromatic Al-Kα radiation source (ESCALAB 250 XI, Thermo Fisher Scientific). FT-IR for C=O stretch, C≡N stretch, and N–H stretch were obtained by a 670-IR (Agilent) spectrophotometer.

Mott–Schottky plots and EIS measurement

Mott–Schottky plots of devices were measured under a bias of 1.02 V. The frequency (1 kHz) was applied with scan rate of 0.02 V S^{-1} using impedance analyzer (SI1260, Solartron). ESI measurements were carried out by an impedance analyzer (SI1260, Solartron).

Conductivity measurement

Parallel Au electrodes were formed on the silicon substrate, and each perovskite film (control or CY-incorporated perovskite) was spin-coated on the Au-patterned substrate. Then, voltage-sourced two-point conductivity was measured with a probe station under dark and atmospheric condition (RH of 30% and 27°C). The electrical conductivity (σ) was calculated using the following equation, $\sigma = (J/V) \times L/(w \times d)$, where L is the channel length, w is the width between the Au electrodes, and d is the thickness of the perovskite films.

Charge carrier mobility measurement

The trap density (N_t) and mobility (μ) values are obtained using the following equations[2],

$$N_t = \frac{2\varepsilon_0 \varepsilon_r V_{TFL}}{qL^2} \quad \text{and} \quad J = \frac{9}{8}\varepsilon_r \varepsilon_0 \mu_h \frac{V^2}{L^3}, \text{ respectively,}$$

where V_{TFL} is a trap-filled limit voltage, ε_0 is the vacuum permittivity, ε_r is a relative dielectric constant of perovskite, L is the thickness of the perovskite film, q is the elementary charge, J is an injection current, and V is a bias voltage. SCLC was measured applying bias to hole-and electron-only devices. The devices were fabricated with the configuration of ITO/ poly[bis(4-phenyl)(2,4,6-trimethylphenyl)amine/perovskite/Spiro-OMeTAD/Au (hole-only device) and ITO/SnO2/perovskite/PC61BM/Au (electron-only device).

Non-radiative voltage loss measurement

EQE_{EL} measurements were performed by applying external voltage/current sources through the devices (ELCT-3010, Enlitech). The non-radiative recombination loss (ΔV_{oc}^{nonrad}) was quantified using the external quantum efficiency electroluminescence (EQE_{EL}) with the following relation[3]:

$$\Delta V_{oc}^{nonrad} = \frac{k_B T}{q} \ln\left(\frac{1}{EQE_{EL}}\right)$$

, where k_B, T, and q is the Boltzman constant, temperature, and elementary charge.

Analysis of ultrafast carrier dynamics

UV-Vis absorption measurement. UV absorption spectra were performed with a UV-2600 spectrometry (Shimadzu) with halogen and deuterium lamps.

PL spectroscopy measurement. Edinburgh spectrophotometer (FLS-920, Edinburgh Instruments, UK) was used for steady-state and time-resolved PL measurements. The samples were excited with a 510-nm laser (EPL-510, Edinburgh Instruments, UK) at a repetition rate of 1 MHz. Excitation fluence was 10 nJ/cm^2. IRF was 1.7 ns. An emission polarizer set to the magic angle of 54.7° from the polarization of the excitation laser. The measurements were performed in air at room temperature.

fs-TA spectroscopy measurement. Femtosecond pulses of 170 fs duration at 1,030 nm were generated by a regenerative amplifier seeded by a mode-locked oscillator (PHAROS, Light Conversion, Lithuania). The femtosecond pulses at a repetition rate of 200 kHz (6 W) were split into two parts. One was used to pump an optical parametric amplifier (ORPHEUS, Light Conversion, Lithuania) to generate wavelength-tunable excitation pulses, and the other was focused into a sapphire crystal to produce a supercontinuum white light in a TA spectrometer (HARPIA, Light Conversion, Lithuania). The excitation and probe beams were focused on samples with a full width at half maximum of 200 and 100 μm, respectively. The pump and probe beams are made to overlap non-colinearly in space and the polarization of the pump beam is set at the magic angle (54.7°) with respect to that of the probe. The transmitted probe beam was collimated and routed to a detector. Here, the white light was spectrally dispersed by a spectrograph (Kymera 193i-B2, Andor, UK), employing selective gratings of 150 lines/mm, blazed at 500. The pump-probe time delay was controlled by a motorized delay stage, and the signal was recorded using the lock-in detection scheme with a chopping frequency of 150 Hz. IRF was 230 fs. The measurements were performed in air at room temperature.

Contact angle measurement and stability tests

Contact angle measurements were performed using the Phoenix 300 Model instrument. For the stability tests, devices were stored in temperature and humidity control chambers to expose each condition consistently (85% RH, 25℃ and 85℃, 85% RH). Measurement during the stability test, the devices were transported to an N_2-filled glove box using a portable vacuum chamber to avoid exposure to irregular environmental conditions. The operational stability tests were conducted in a nitrogen-filled glovebox. Maximum Power Point (MPP) tracking tests were performed on encapsulated devices under AM 1.5G (100 mW cm^{-2}) LED illumination at 25 °C and 50% relative humidity (T3600, 298 McScience), where the devices were encapsulated using glass-to-glass encapsulation using UV-curable adhesive as a sealant.

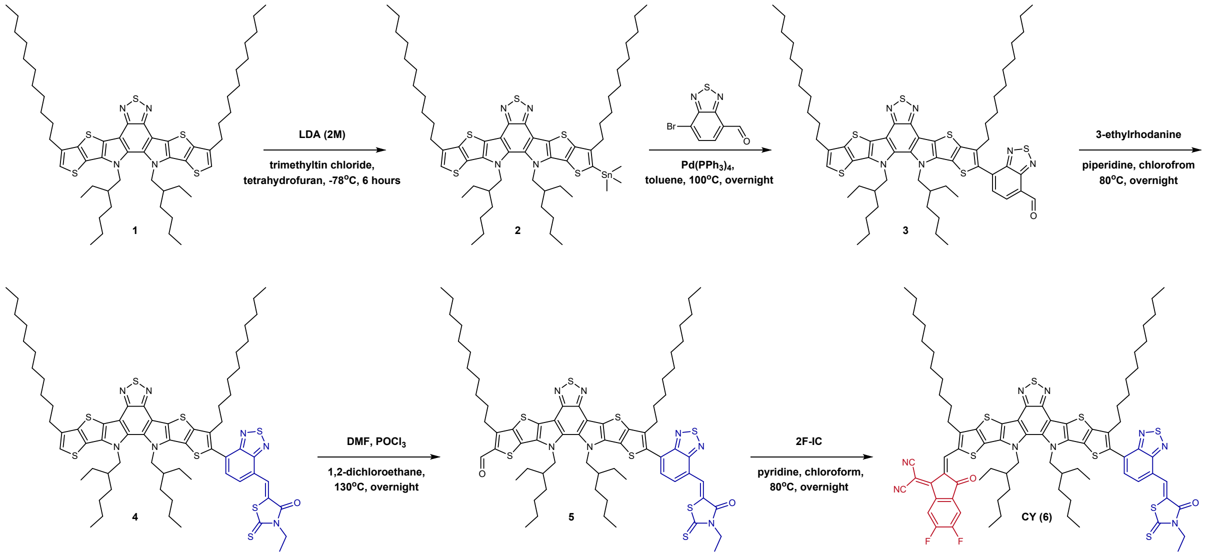

Figure S1. Synthetic route of CY.

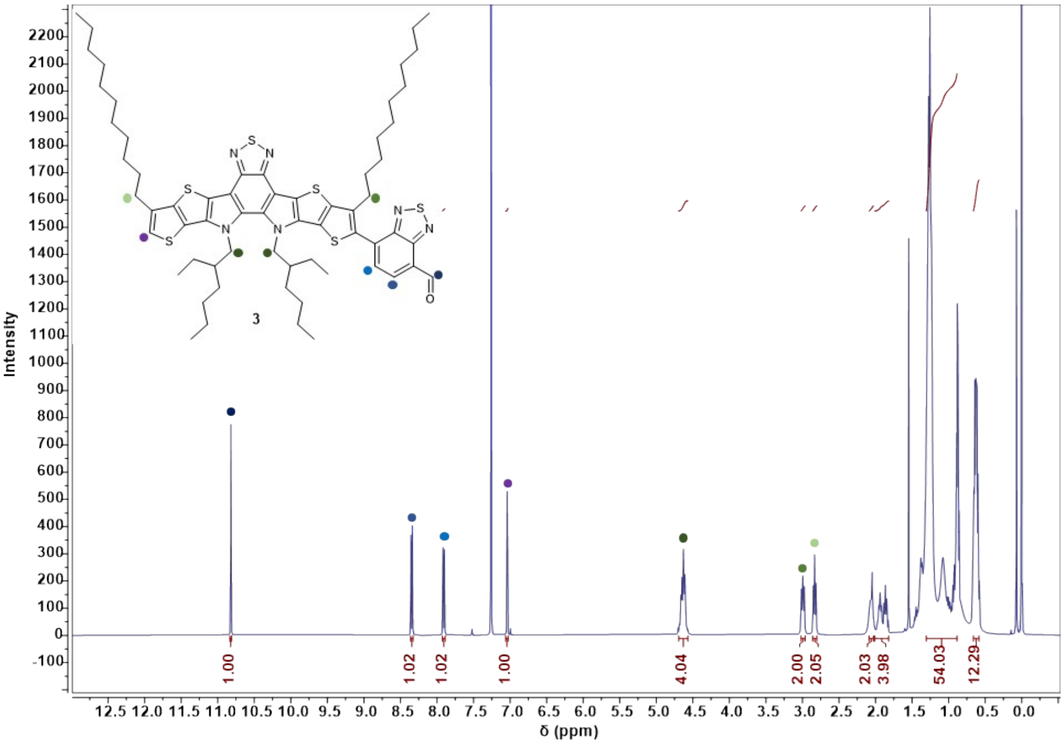

Figure S2. ^{1}H NMR spectra of material 3.

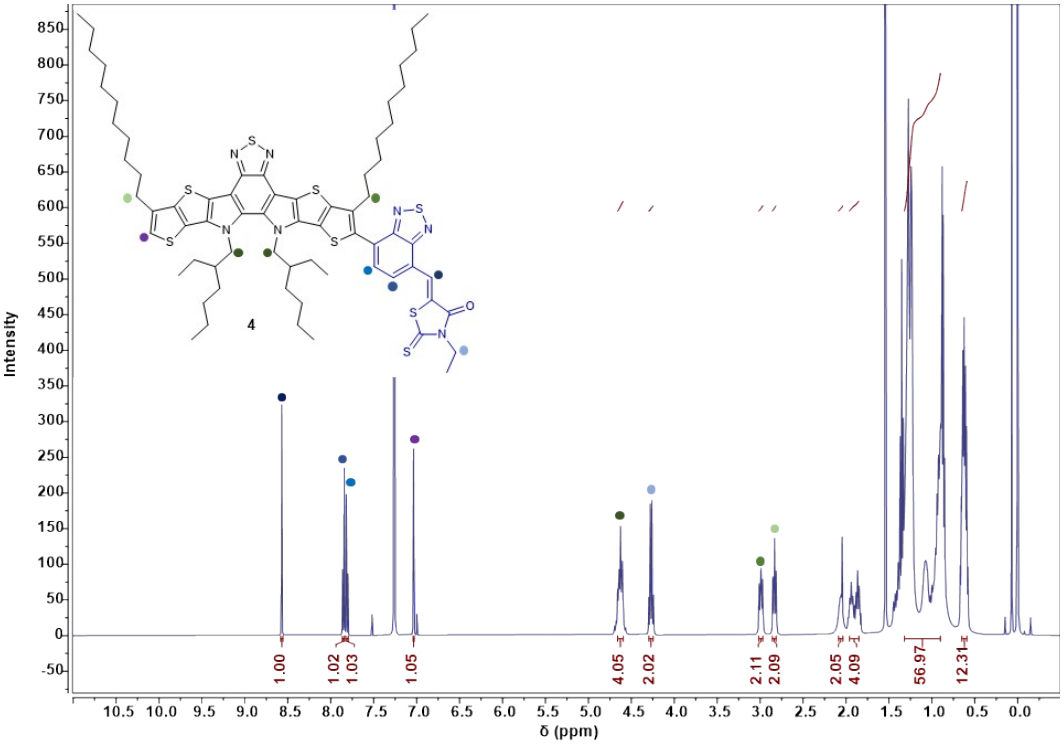

Figure S3. ^{1}H NMR spectra of material 4.

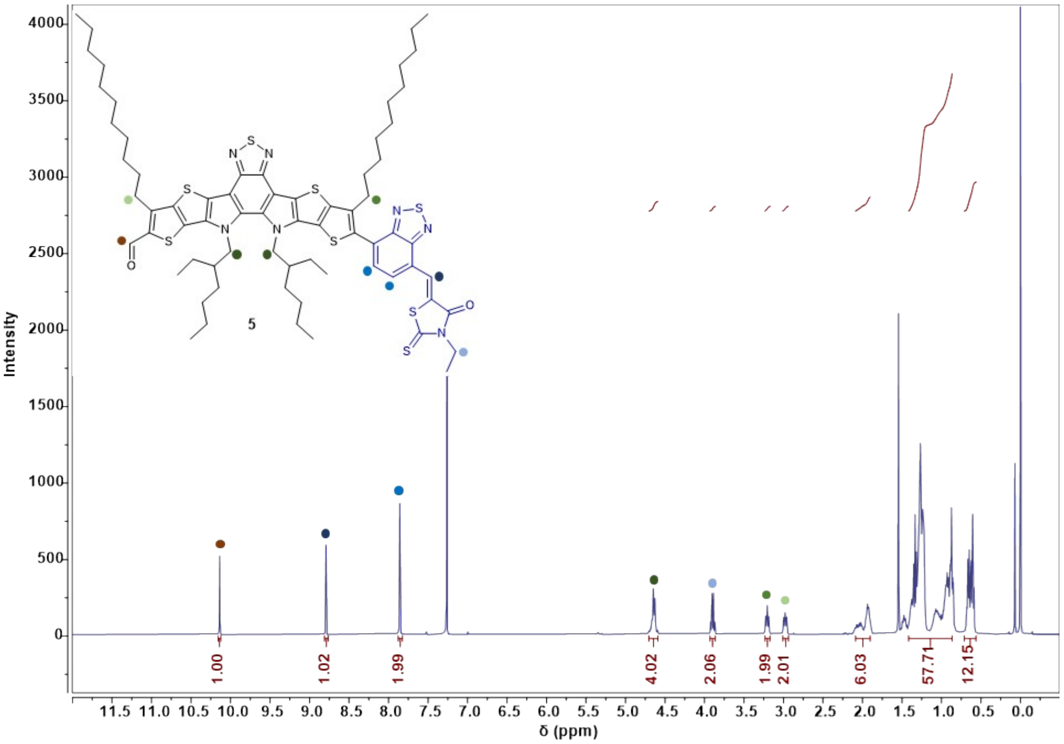

Figure S4. ^{1}H NMR spectra of material 5.

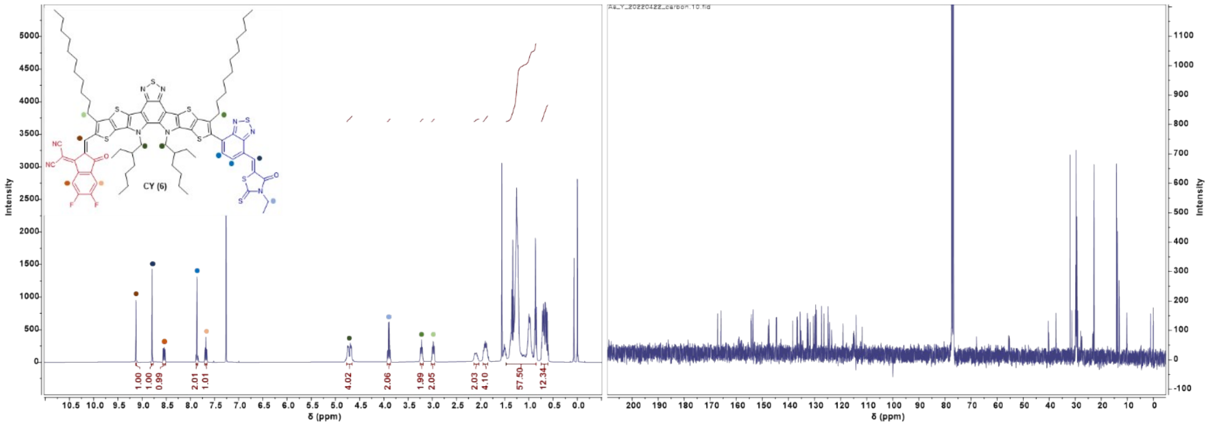

Figure S5. ^{1}H NMR spectra and ^{13}C NMR spectra of CY.

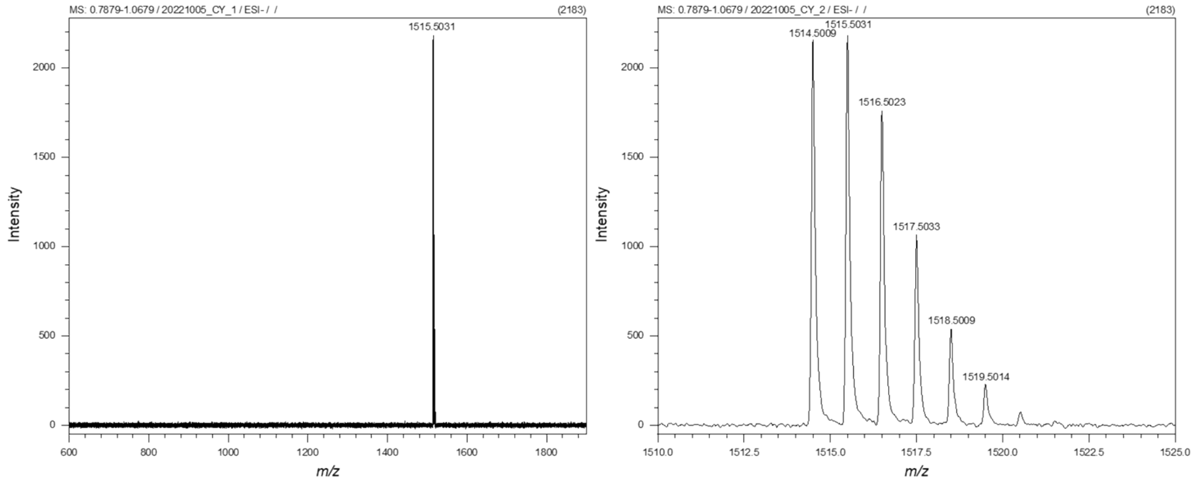

Figure S6. HRMS spectra of CY.

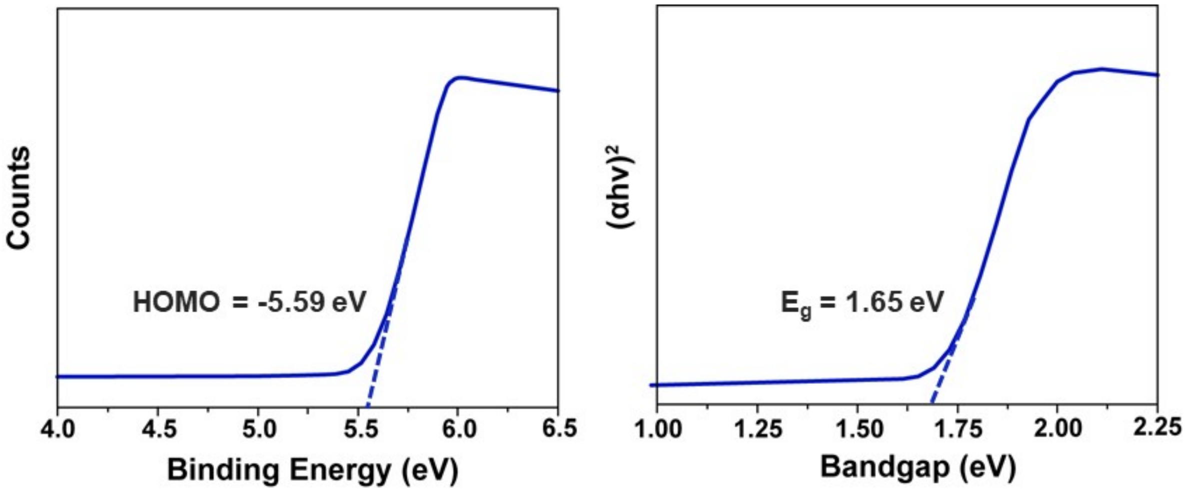

Figure S7. (left) UPS spectra and (right) Tauc plot of pristine CY film.

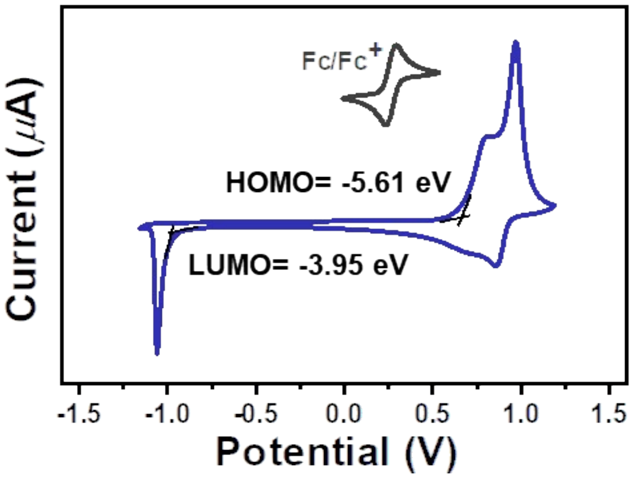

Figure S8. CV curve, and calculated HOMO and LUMO levels of pristine CY film.

Table S1. Summary of quantitative information of ESP distributions and polarity of CY, Y6, and IT-4F (Isosurface = 0.001 au).

	Overall surface area [Å^2]	**Negative ESP surface area [%]**	**Molecular polarity index [kcal/mol]**	**Minimal negative ESP [kcal/mol]**	**Maximal positive ESP [kcal/mol]**	**Net dipole moment [Debye]**
CY	879.37	31.78	12.01	-37.38	40.90	7.64
Y6	812.20	30.92	11.16	-35.17	43.23	1.18
IT4F	1106.83	29.29	9.46	-36.15	27.70	0.14

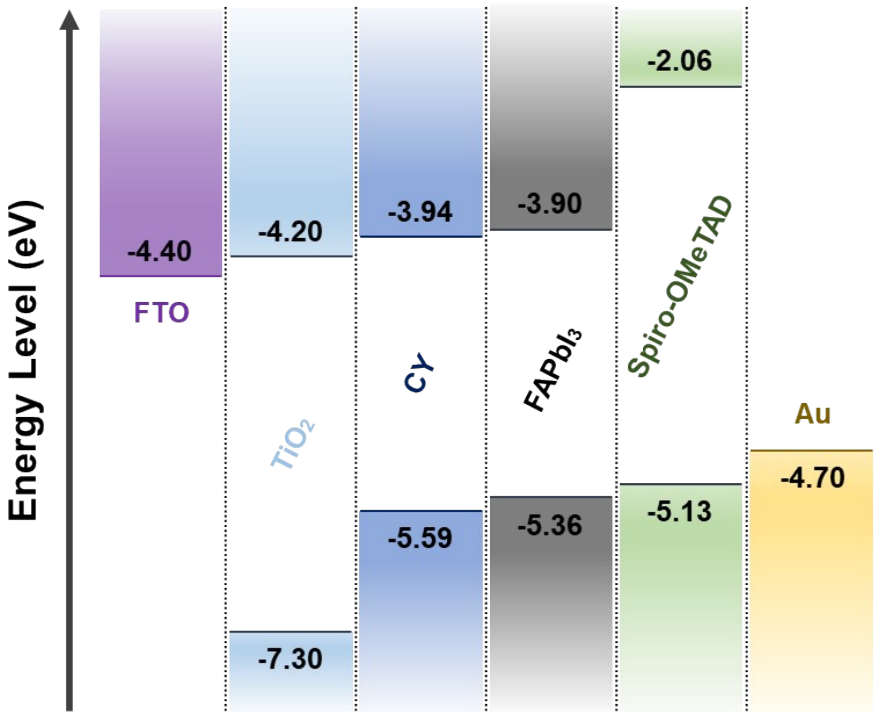

Figure S9. Energy level diagram of PSC components.

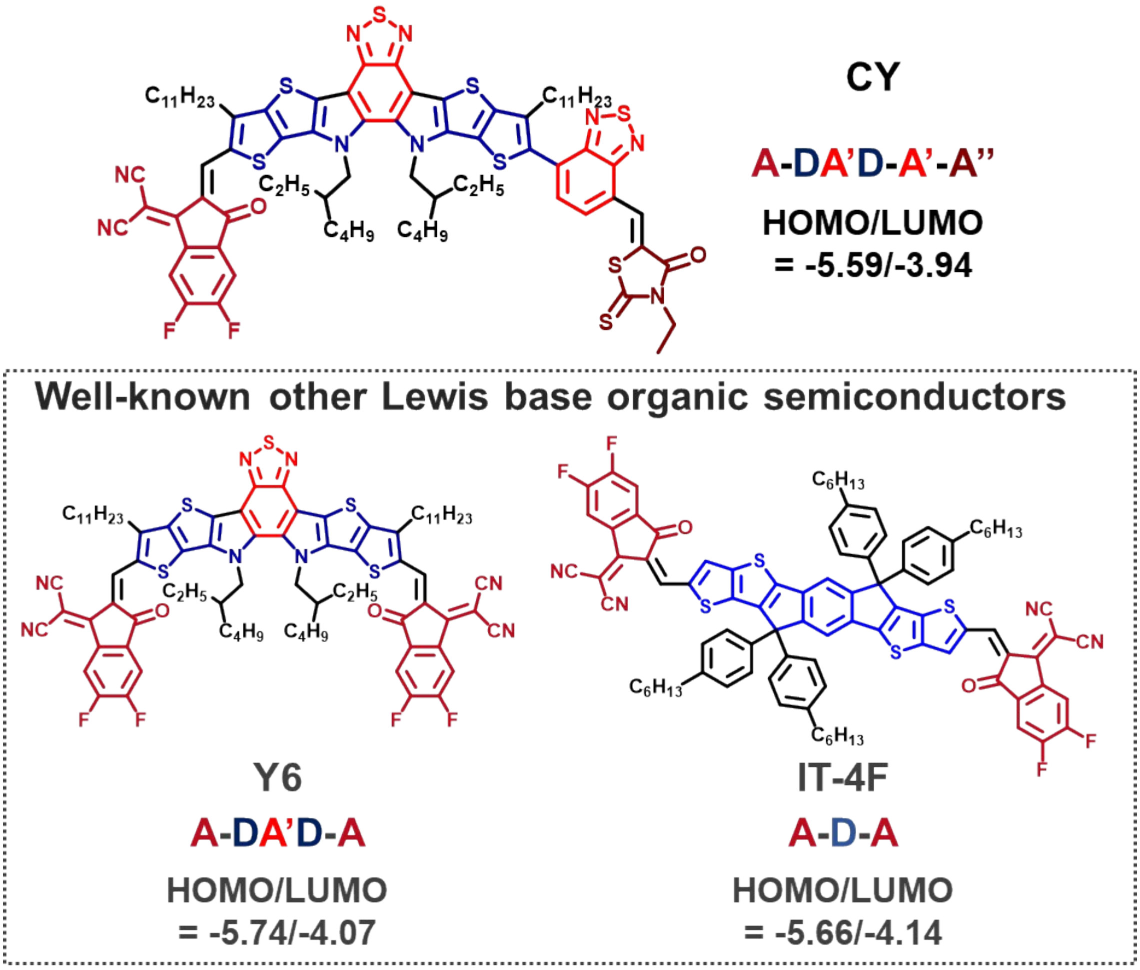

Figure S10. Chemical structure, push-pull architecture, and HOMO and LUMO energy levels of CY, Y6, and IT-4F.

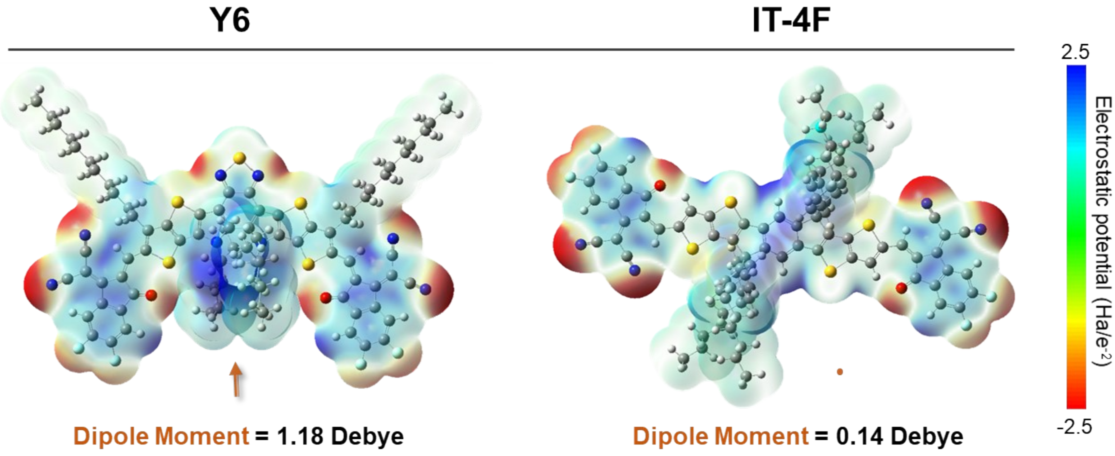

Figure S11. ESP distributions and dipole moments of Y6 and IT-4F calculated by DFT.

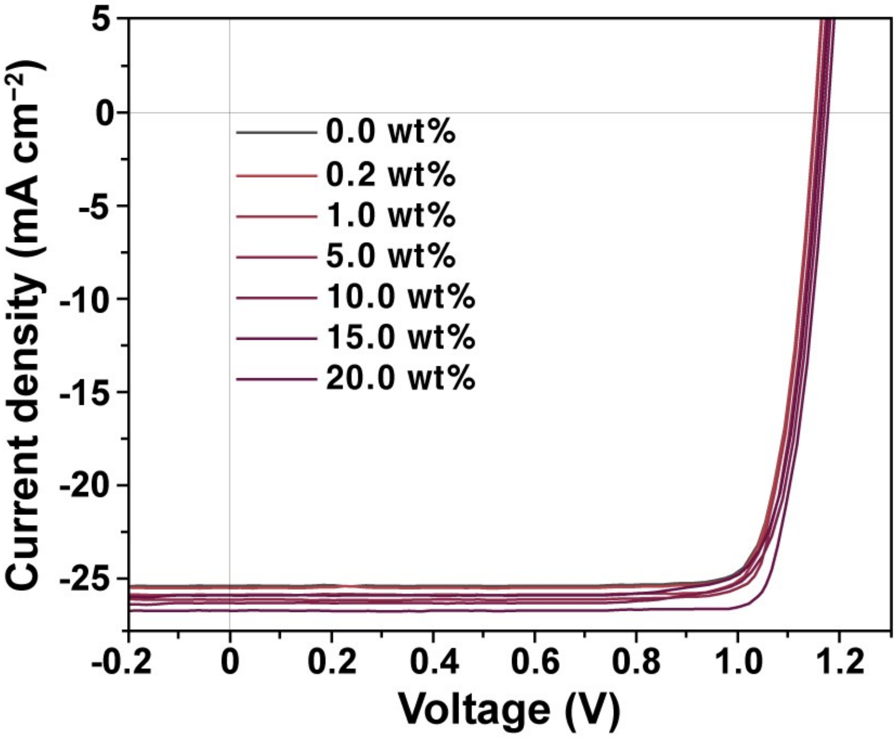

Figure S12. *J*–*V* characteristics of PSCs with the different weight ratio of CY.

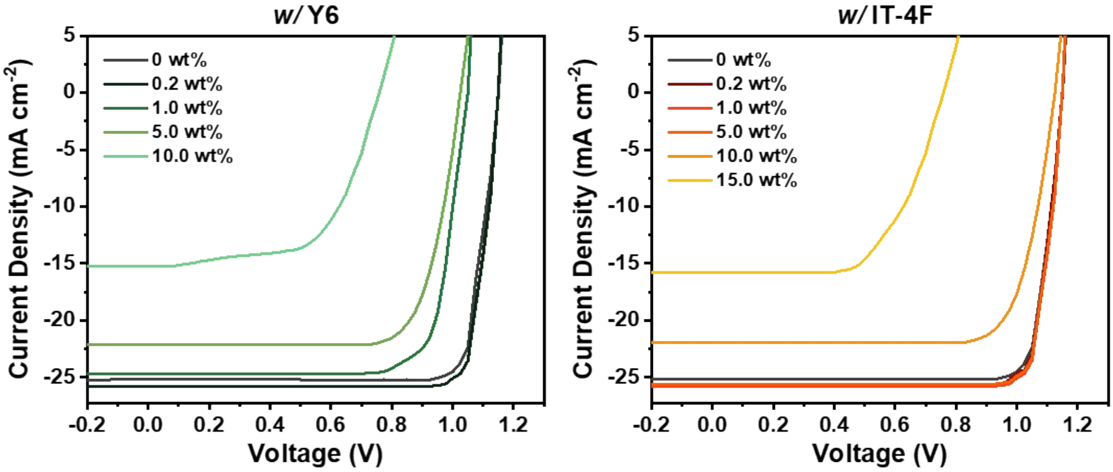

Figure S13. *J*–*V* curves of PSCs with different ratios of Y6 and IT-4F.

Table S2. Photovoltaic parameters of PSCs with the different weight ratios of Y6 and IT-4F.

Weight ratio of Y6		J_{sc} [mA cm^{-2}]	V_{oc} [V]	FF [%]	PCE [%]
0 wt%	R	25.2	1.13	80.8	23.0
0.2 wt%	R	25.8	1.15	81.8	24.3
1.0 wt%	R	24.7	1.07	79.2	20.9
5.0 wt%	R	22.1	1.03	76.9	17.5
10.0 wt%	R	15.3	0.76	68.3	7.9
15.0 wt%		Device not working			
20.0 wt%		Device not working			

Weight ratio of IT-4F		J_{sc} [mA cm^{-2}]	V_{oc} [V]	FF [%]	PCE [%]
0 wt%	R	25.3	1.14	80.5	23.2
0.2 wt%	R	25.6	1.15	81	23.8
1.0 wt%	R	25.8	1.15	81.9	24.3
5.0 wt%	R	25.8	1.15	81.1	24.1
10.0 wt%	R	21.8	1.12	76.5	18.7
15.0 wt%	R	15.8	0.76	62.3	7.5
20.0 wt%		Device not working			

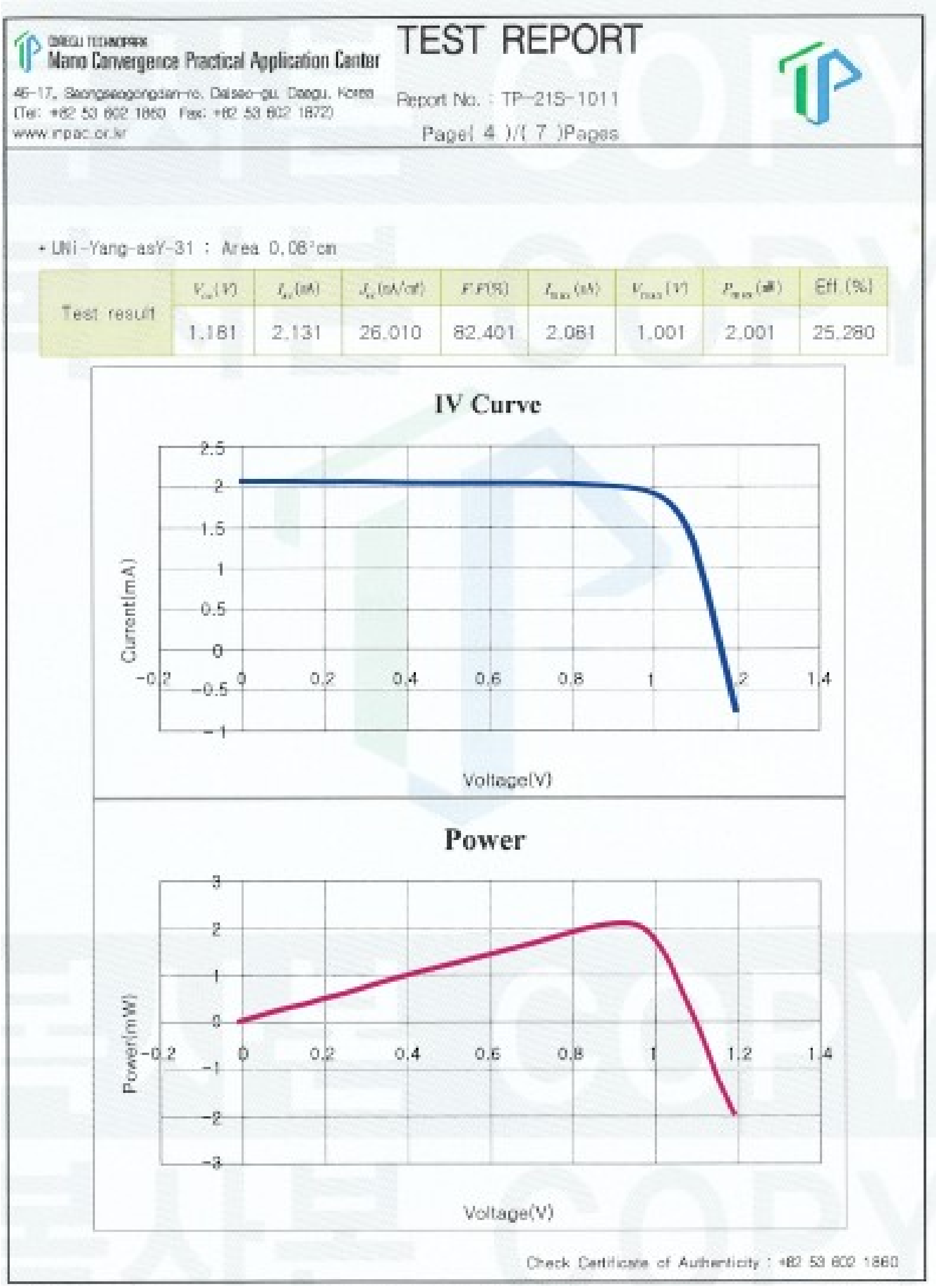

DAEGU TECHNOPARK
Nano Convergence Practical Application Center
46-17, Seongseogongdan-ro, Dalseo-gu, Daegu, Korea
(Tel: +82 53 602 1860 Fax: +82 53 602 1872)
www.inpac.or.kr

TEST REPORT

Report No. : TP-21S-1011
Page(4)/(7)Pages

- UNi-Yang-asY-31 : Area 0.08^{2}cm

	V_{oc} (V)	I_{sc} (mA)	J_{sc} (mA/cm²)	F.F(%)	I_{max} (mA)	V_{max} (V)	P_{max} (mW)	Eff.(%)
Test result	1.181	2.131	26.010	82.401	2.081	1.001	2.001	25.280

IV Curve

Power

Check Certificate of Authenticity : +82 53 602 1860

Figure S14. Certification of CY-incorporated PSC from Nano Convergence Practical Application Center, Republic of Korea.

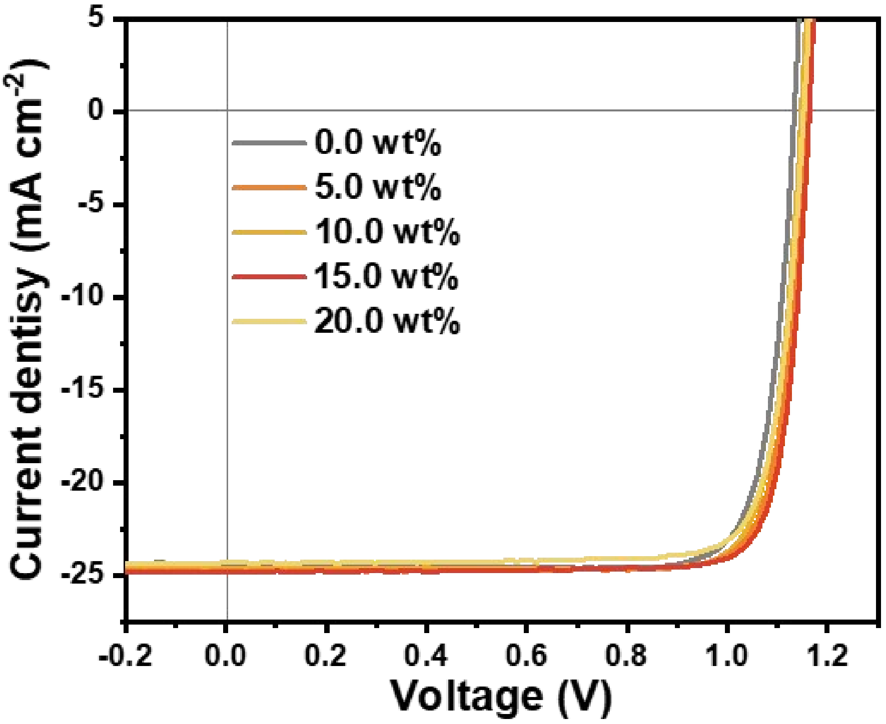

Figure S15. *J–V* curves of the p-i-n structured PSCs with the different weight ratio of CY.

Table S3. Photovoltaic parameters of p-i-n structured PSCs with the different weight ratio of CY.

Weight ratio of CY	J_{sc} [mA cm^{-2}]	V_{oc} [V]	FF [%]	PCE [%]
0 wt% (Control PSC)	24.4 (24.2±0.2)a)	1.13 (1.13±0.01)a)	83.7 (83.5±0.2)a)	23.1 (22.7±0.3)a)
5.0 wt%	24.7 (24.6±0.1)a)	1.15 (1.14±0.02)a)	83.9 (83.8±0.3)a)	23.7 (23.2±0.2)a)
10.0 wt%	24.8 (24.6±0.1)a)	1.154 (1.15±0.03)a)	83.8 (80.5±0.3)a)	24.0 (23.6±0.2)a)
15.0 wt%	24.82 (24.8±0.2)a)	1.161 (1.16±0.03)a)	84.0 (84.0±0.3)a)	24.2 (23.9±0.2)a)
20.0 wt%	24.3 (24.0±0.2)a)	1.150 (1.14±0.03)a)	82.6 (81.4±0.2)a)	23.1 (23.0±0.2)a)

a)The average values and standard deviations obtained from 10 devices.

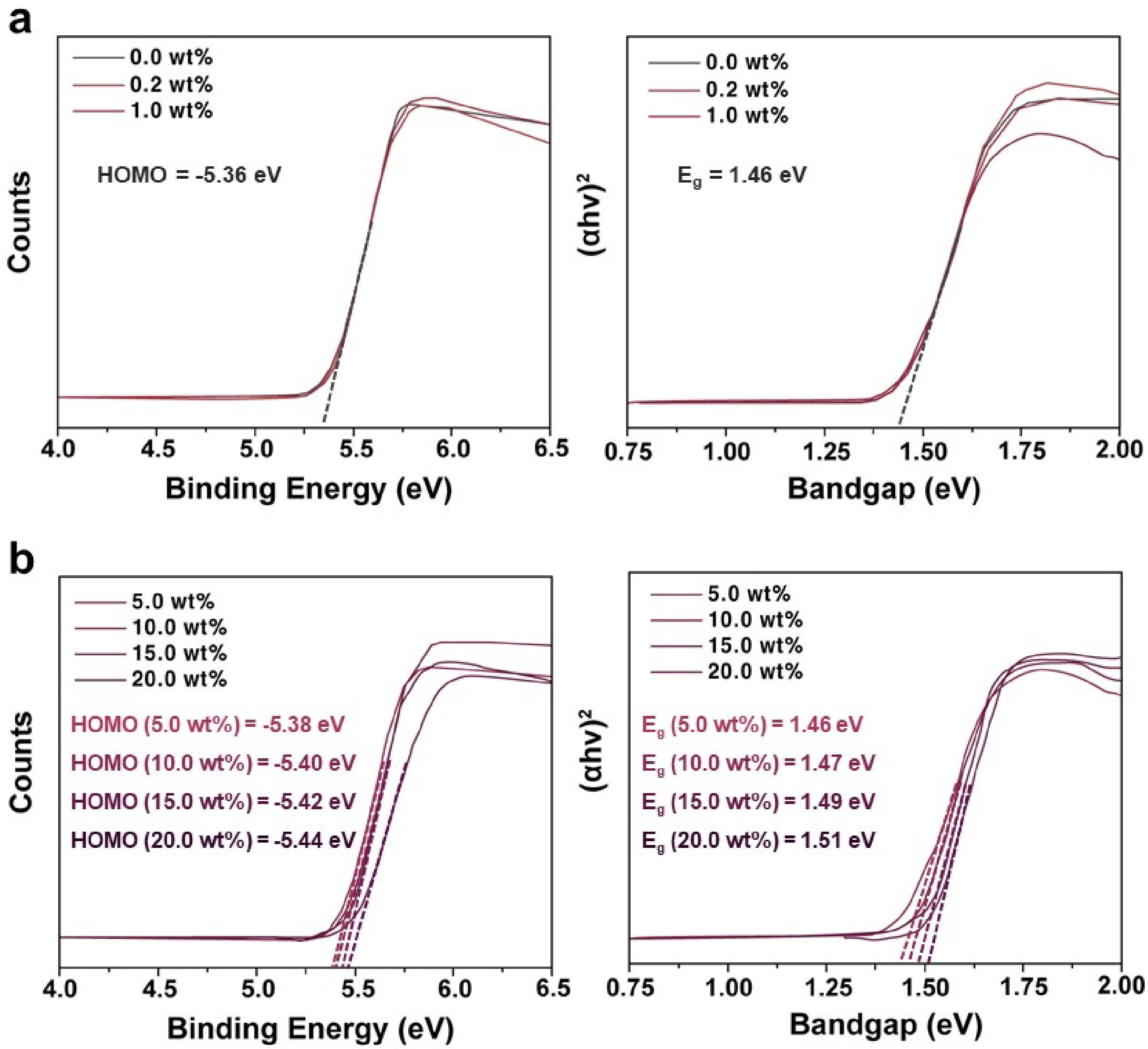

Figure S16. UPS spectra (left) and Tauc plots (right) of perovskite films with (**a**) 0–1.0 wt% and (**b**) 5.0–20.0 wt% of CY.

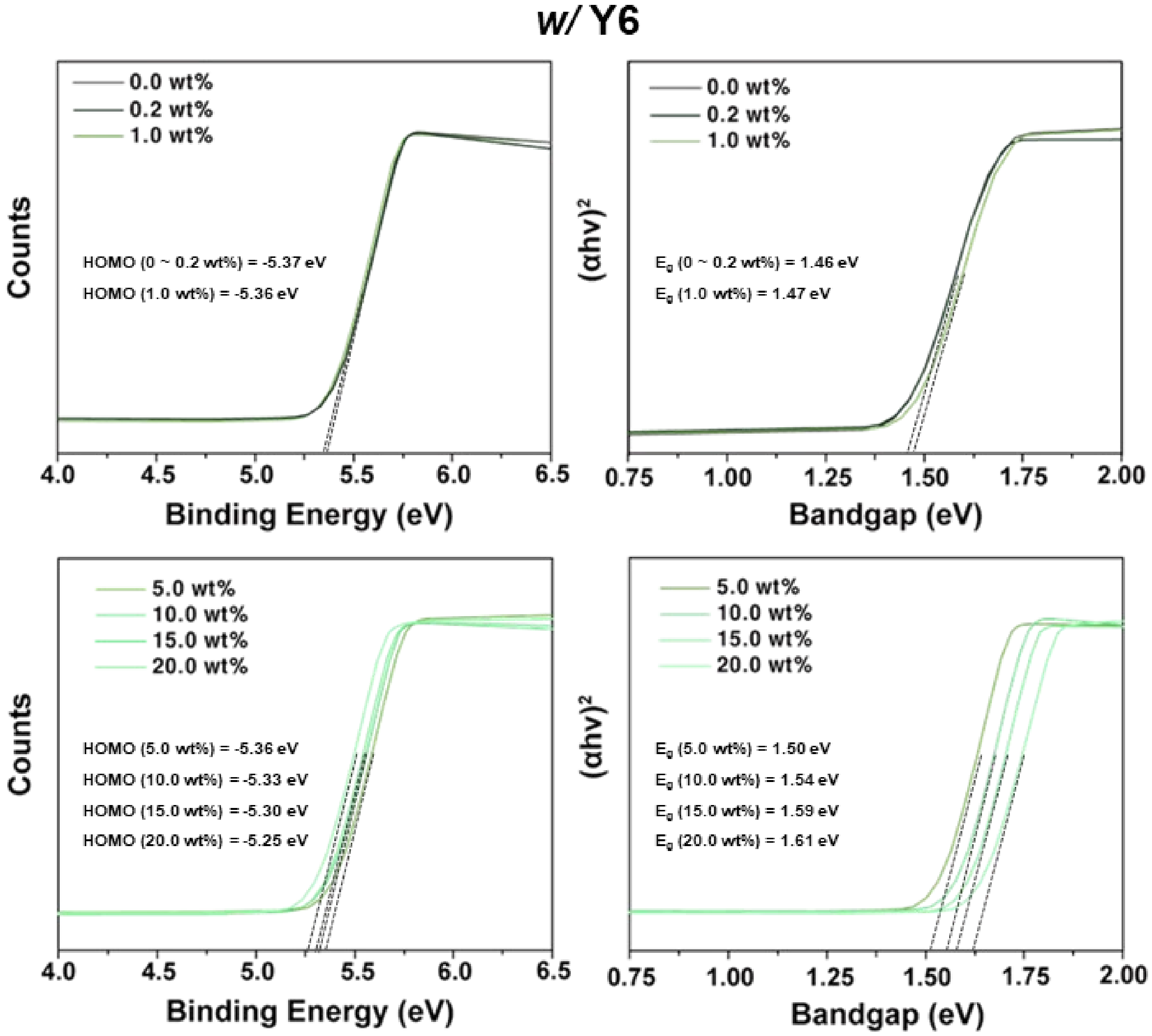

Figure S17. UPS spectra (left) and Tauc plots (right) of perovskite films with (**a**) 0–1.0 wt% and (**b**) 5.0–20.0 wt% of Y6.

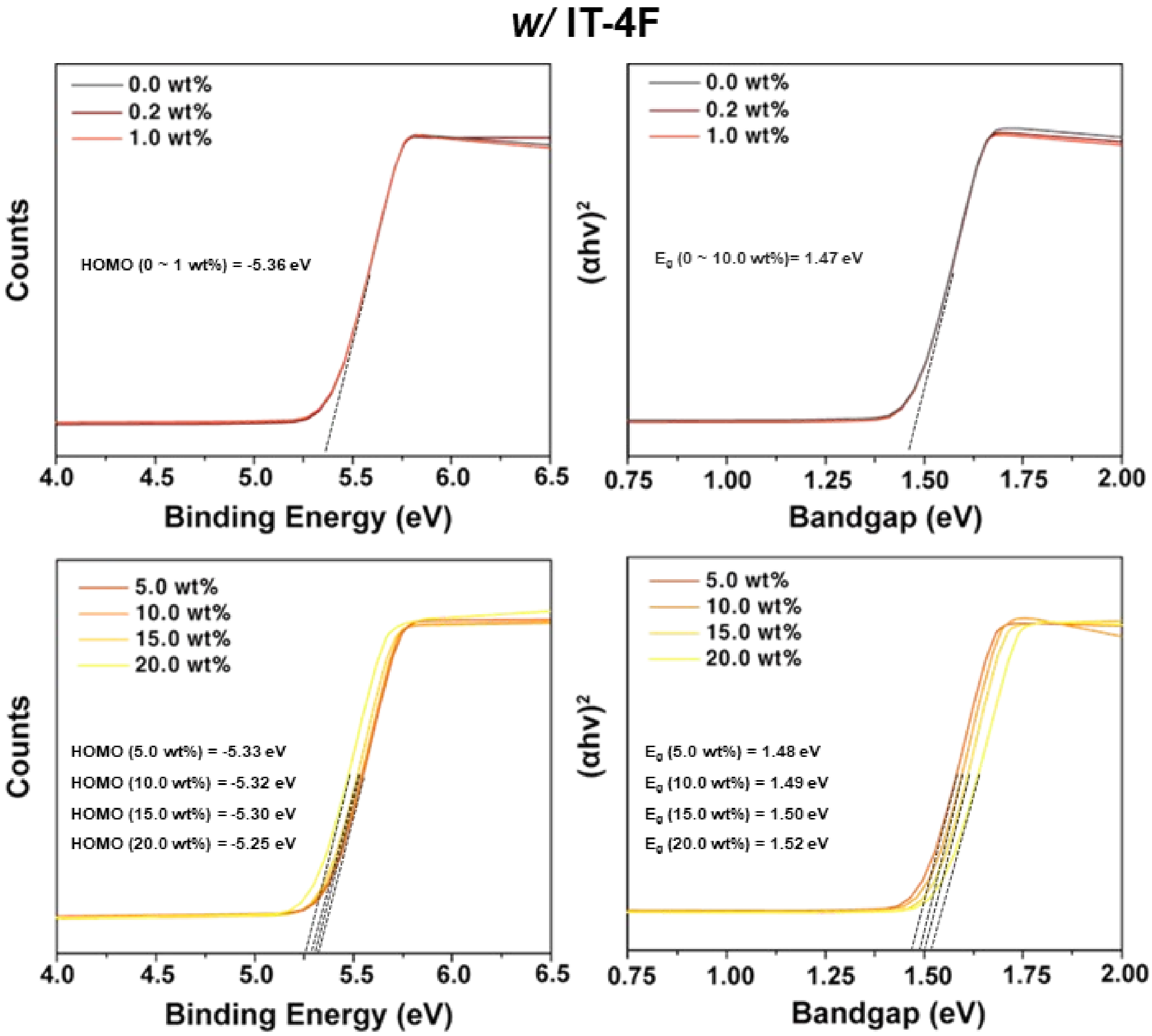

Figure S18. UPS spectra (left) and Tauc plots (right) of perovskite films with (**a**) 0–1.0 wt% and (**b**) 5.0–20.0 wt% of IT-4F.

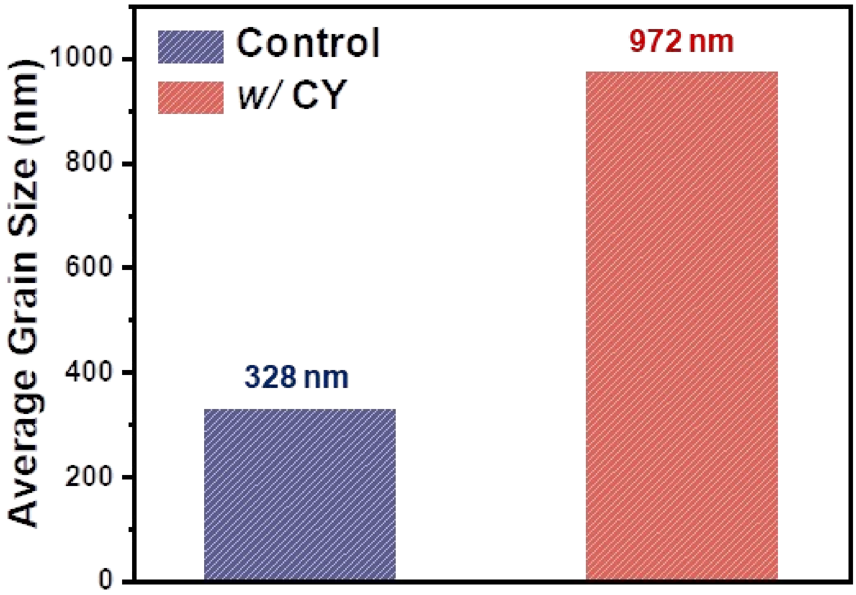

Figure S19. Average grain size of control and CY-incorporated perovskite films.

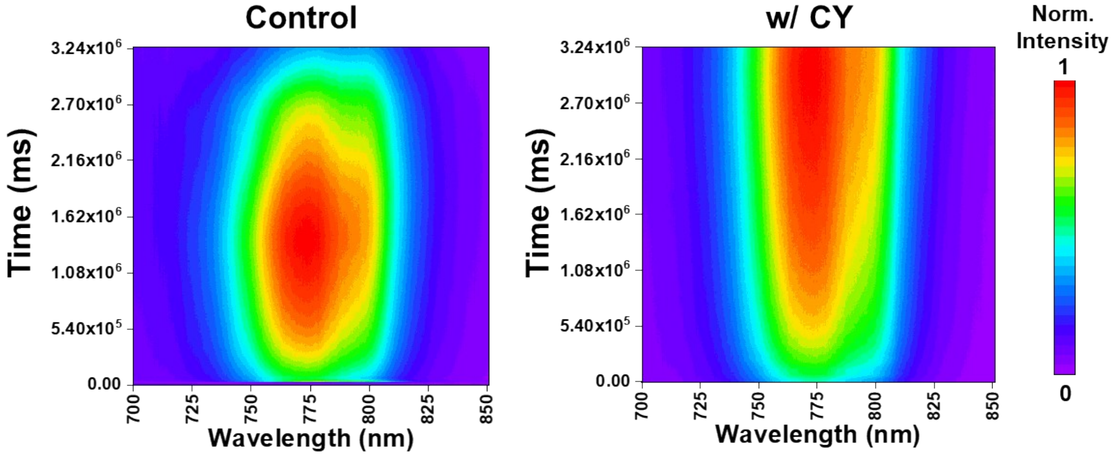

Figure S20. In situ PL spectra of control and CY-incorporated perovskite films during crystallization under thermal annealing at 100°C with 650 nm excitation.

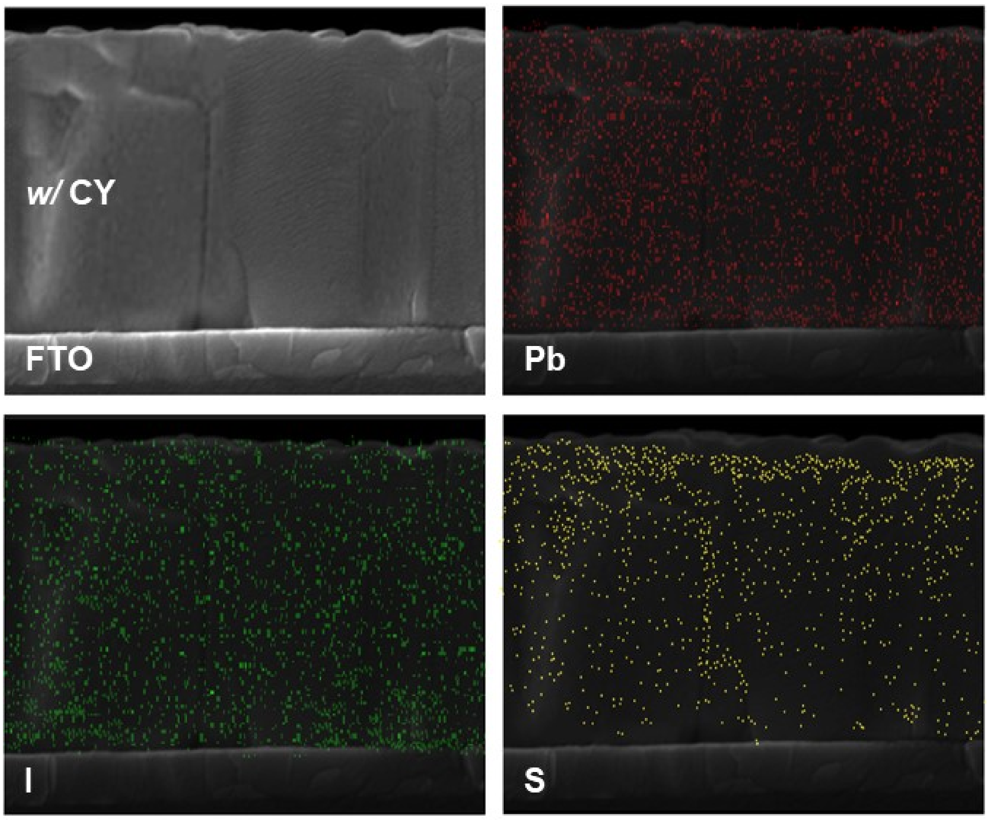

Figure S21. Cross-sectional SEM image and corresponding EDX mapping of CY-incorporated perovskite film.

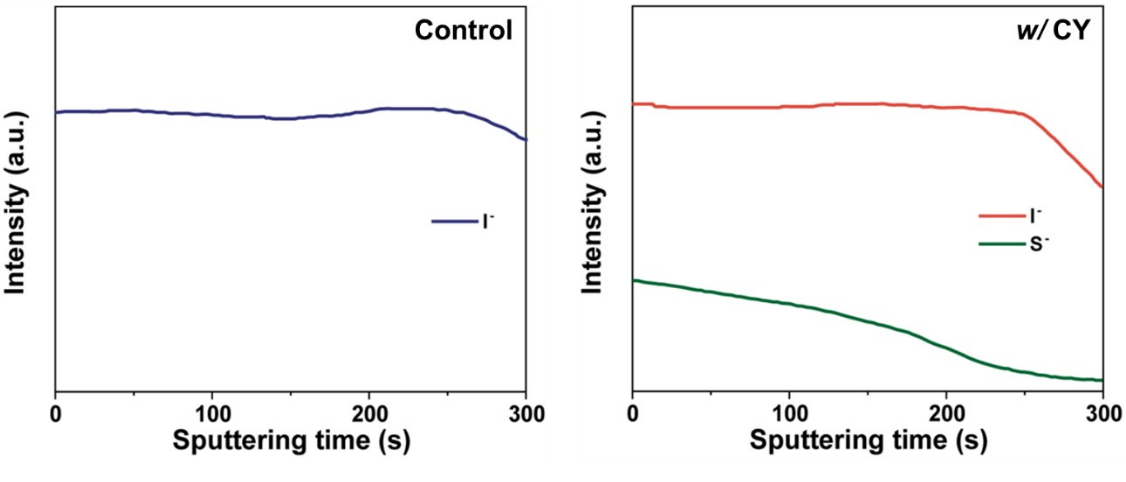

Figure S22. ToF-SIMS of control and CY-incorporated perovskite films.

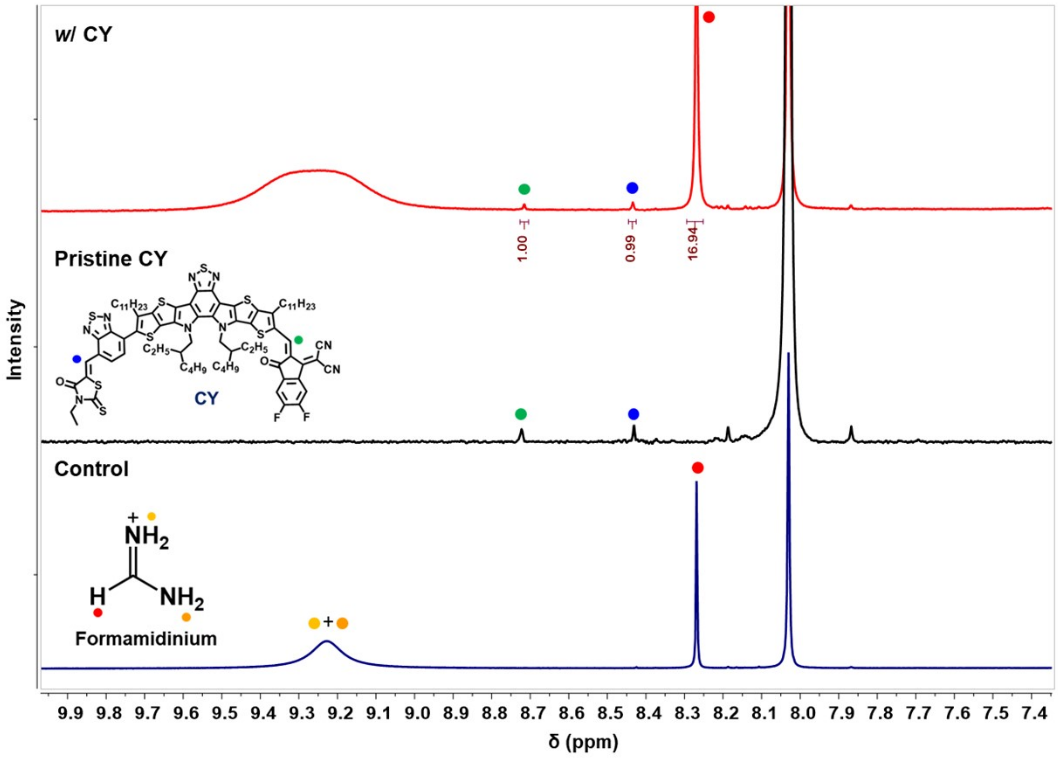

Figure S23. ^{1}H NMR spectra of CY, control perovskite, and 15 wt% CY-incorporated perovskite films in DMF-d$_7$ at 600 MHz.

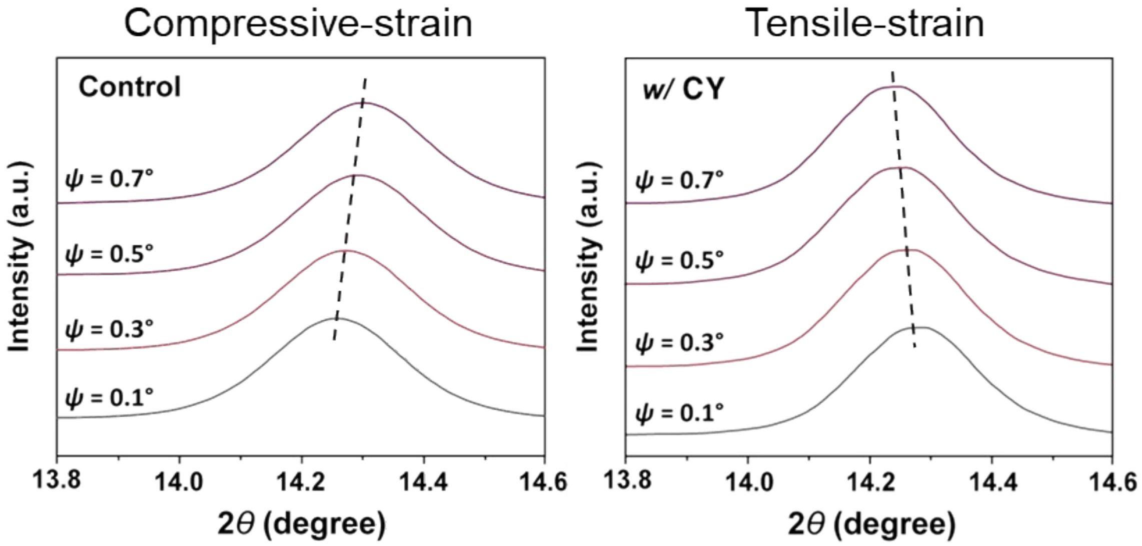

Figure S24. GIXRD with different instrumental values for control and CY-incorporated films.

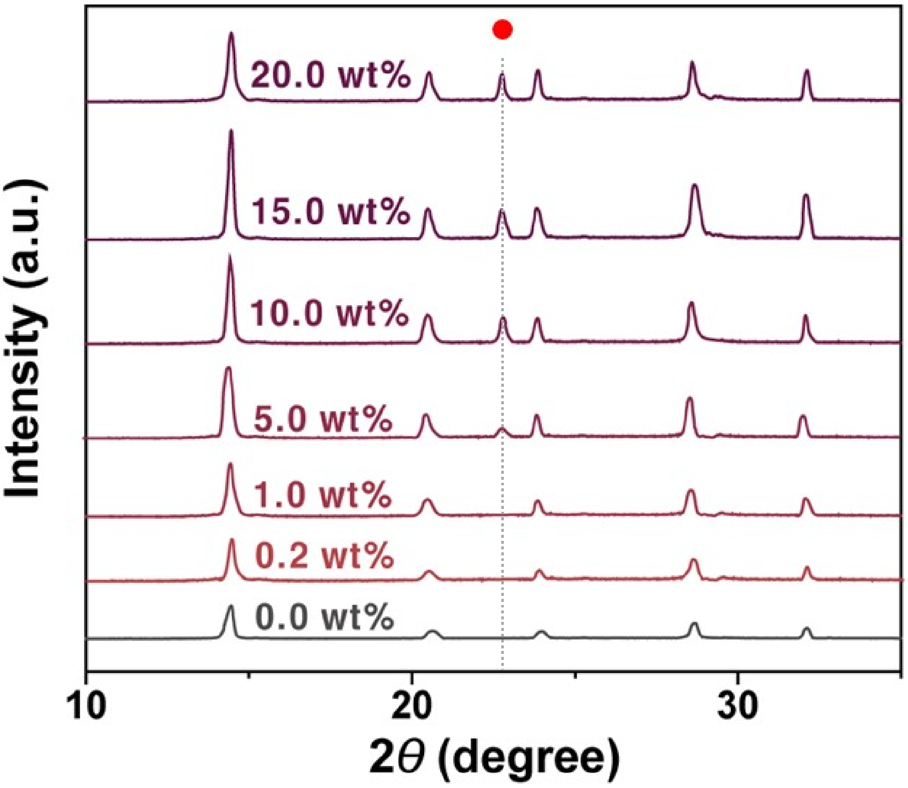

Figure S25. XRD patterns of perovskite films with the different weight ratio of CY.

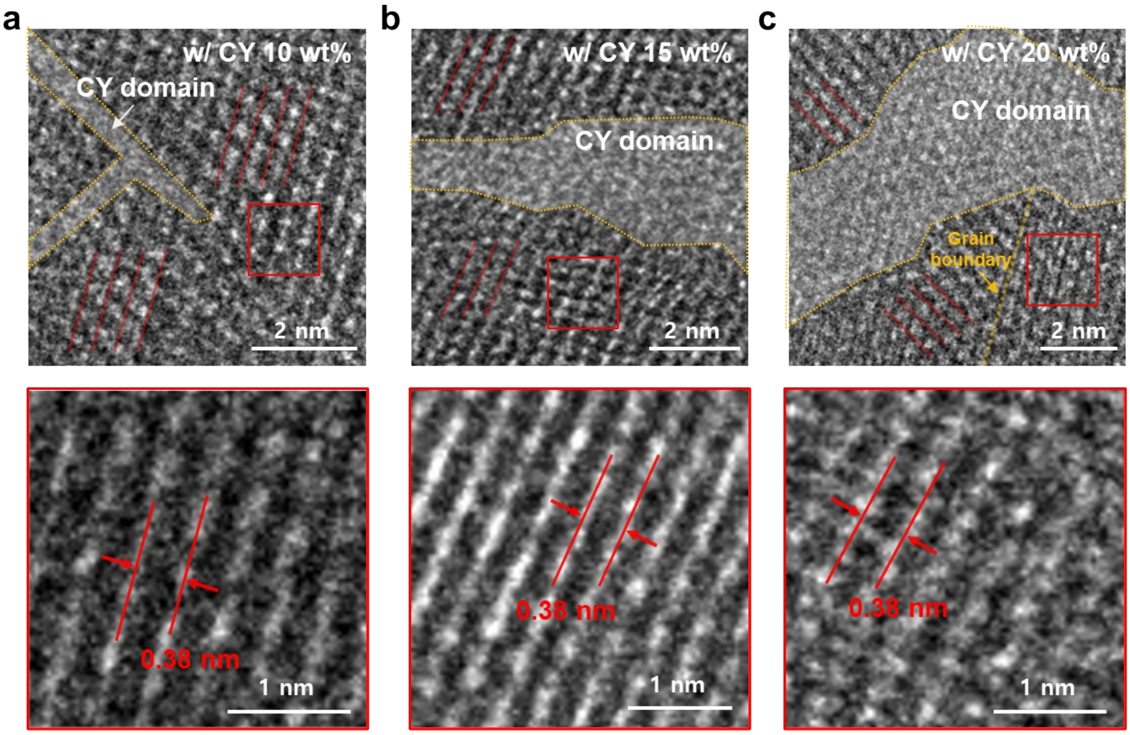

Figure S26. High resolution-TEM images of (**a**) 10 wt%, (**b**) 15 wt%, and (**c**) 20 wt% CY incorporated perovskite films (magnified images in red boxes).

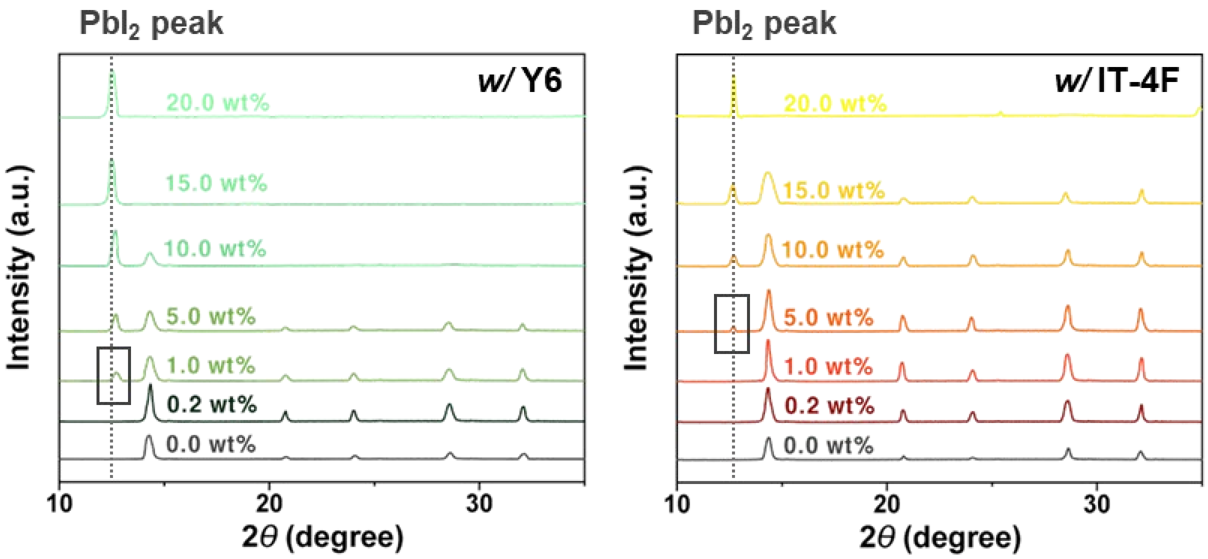

Figure S27. XRD patterns of perovskite films with the different weight ratios of Y6 and IT-4F.

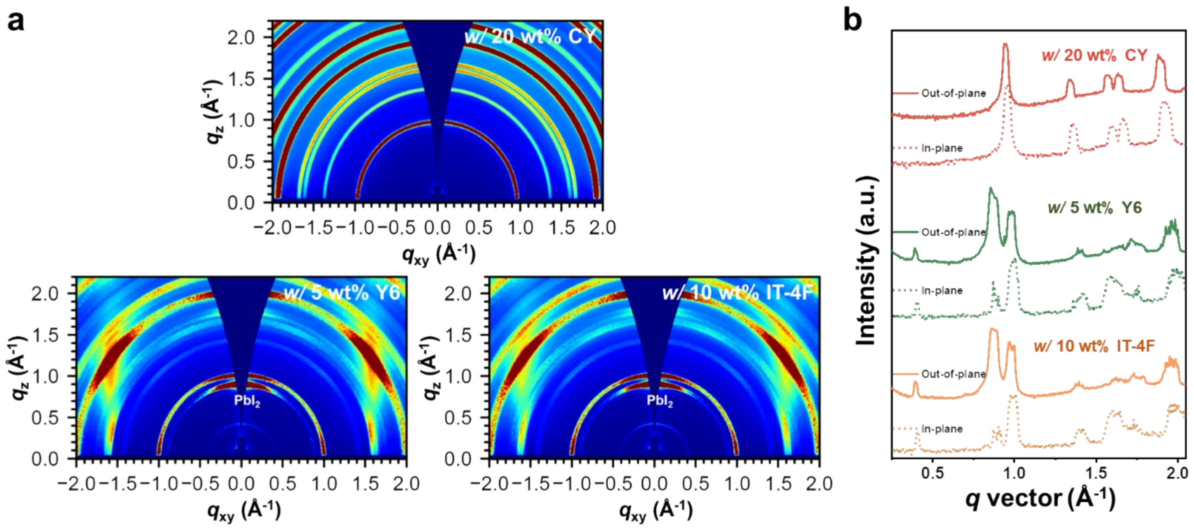

Figure S28. (**a**) Two-dimensional GIWAXS images of excess amount of CY (20 wt%), Y6 (5 wt%), and IT-4F (10 wt%)-incorporated perovskite films, (**b**) and their corresponding line-cut profiles.

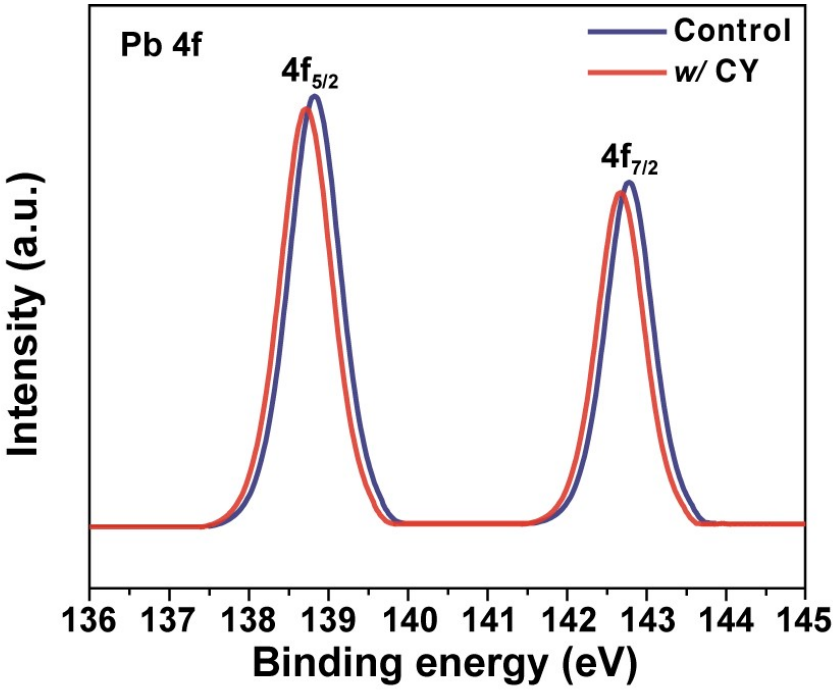

Figure S29. The XPS spectra of Pb 4f in the control and CY-incorporated perovskite films.

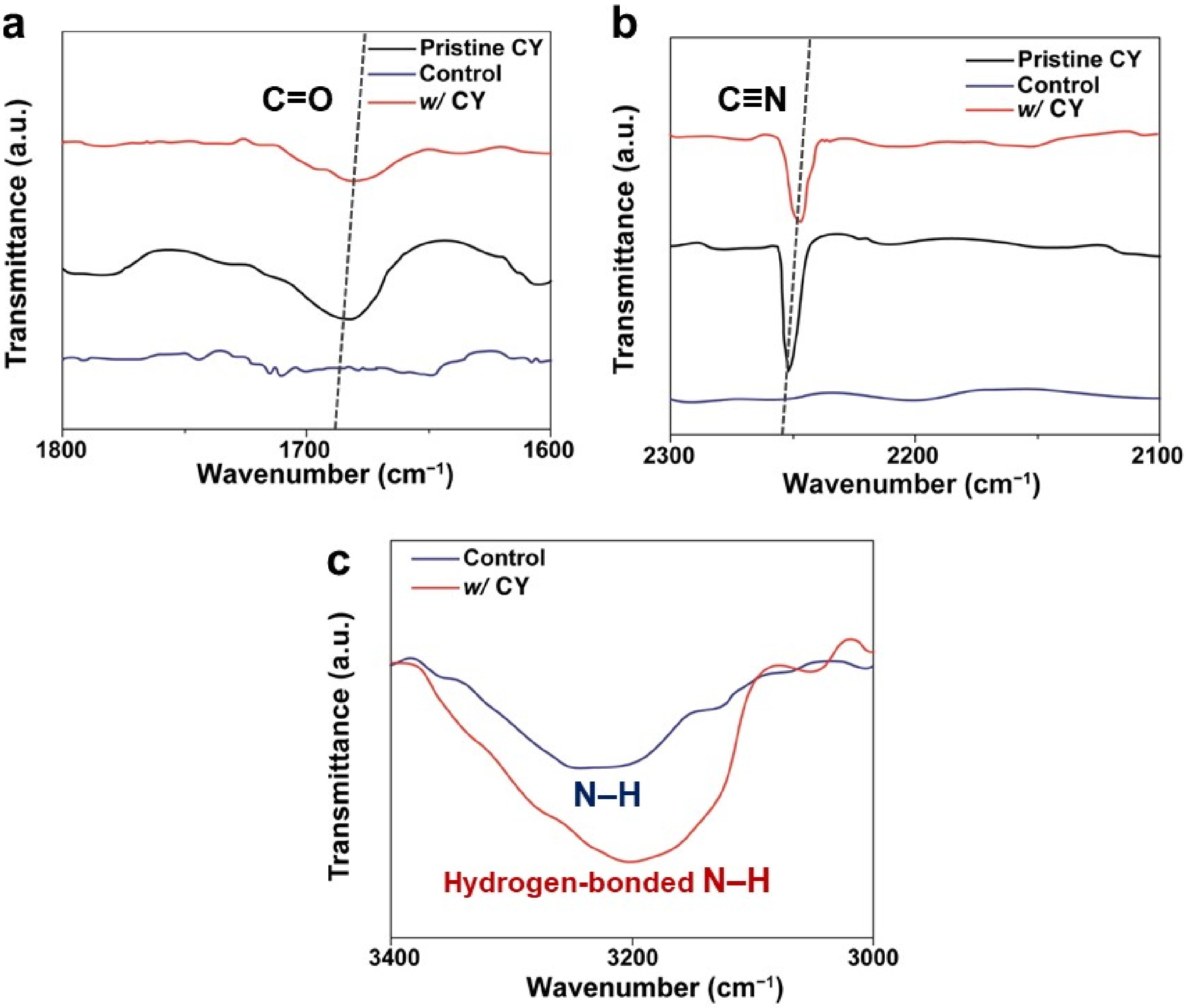

Figure S30. FT-IR spectra of pristine CY, control perovskite, and CY-incorporated perovskite films; (A) C=O stretch peak and (B) C≡N stretch peak. (C) N–<u>*H*</u> stretch peak of control and CY-incorporated perovskite films.

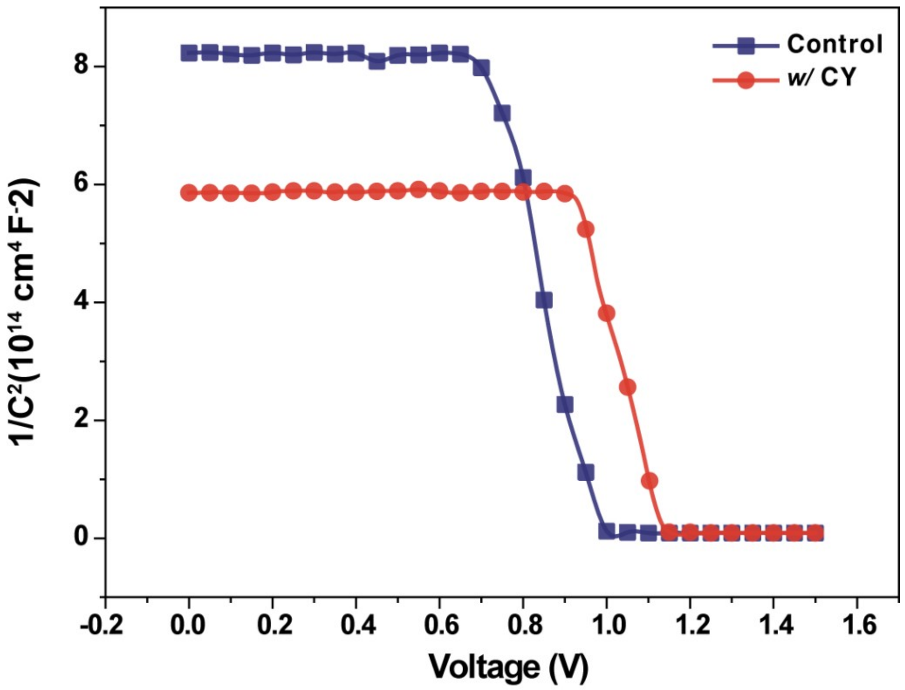

Figure S31. Mott–Schottky plots of control and CY-incorporated PSCs without electron-transport layers (FTO/perovskite/Spiro/Au) at 1 kHz.

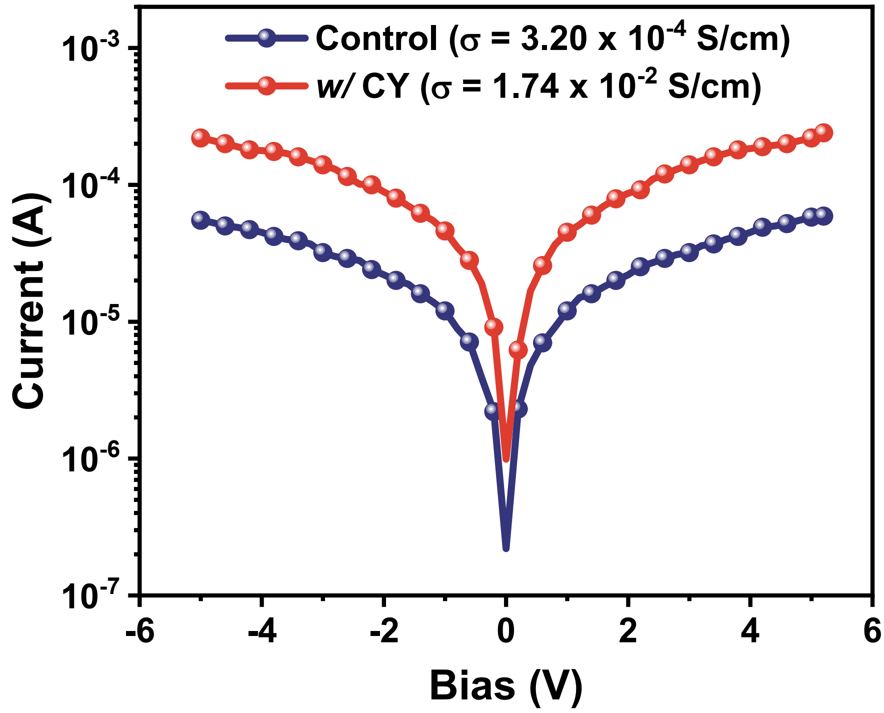

Figure S32. Electrical conductivity of the control and CY-incorporated perovskite films measured with a two-point probe system under dark condition.

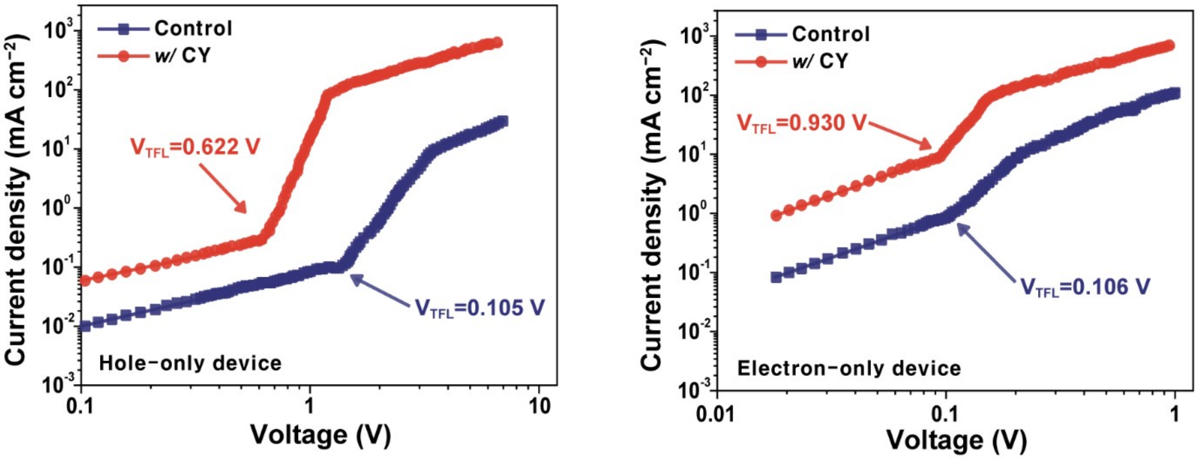

Figure S33. Dark *J*–*V* characteristics of the hole- (left) and electron-only (right) PSCs, indicating the V_{TFL} kink point.

Table S4. Summary of mobilities of control and CY-incorporated PSCs.

Device	μ_h [cm^2 V^{-1} s^{-1}]	μ_e [cm^2 V^{-1} s^{-1}]	N_{th}/N_{te}
Control	7.98×10^{-4}	1.2×10^{-4}	$1.79 \times 10^{16}/5.05 \times 10^{15}$
w/ CY	1.62×10^{-3}	1.13×10^{-3}	$1.18 \times 10^{16}/3.12 \times 10^{15}$

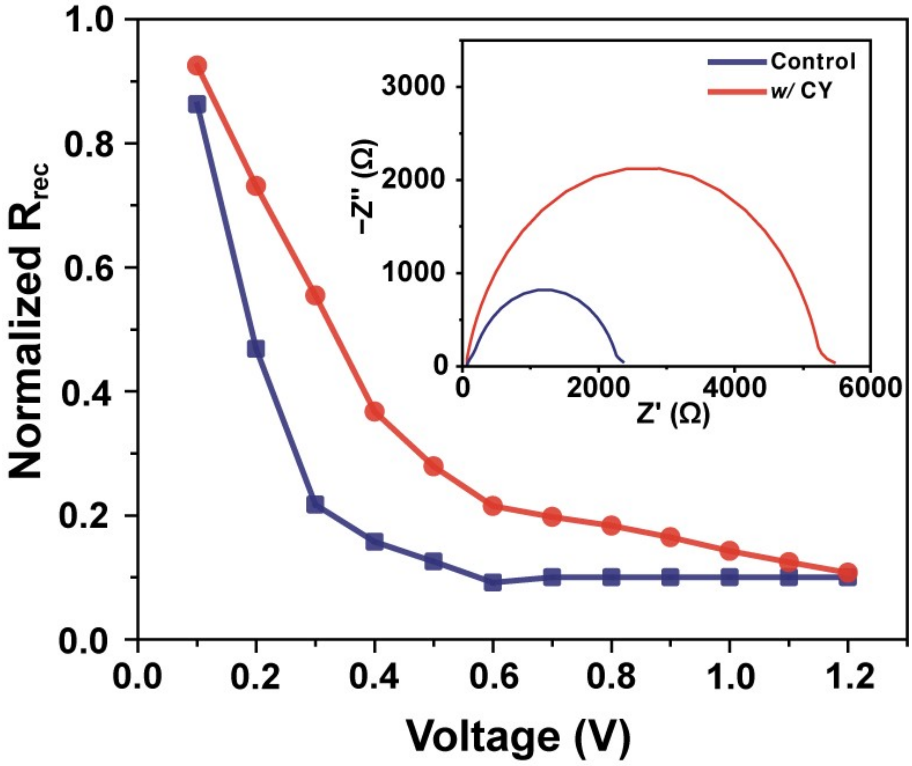

Figure S34. Normalized recombination resistance versus voltage, and Nyquist plots of the EIS measurements (inset) from the control and CY-incorporated PSCs.

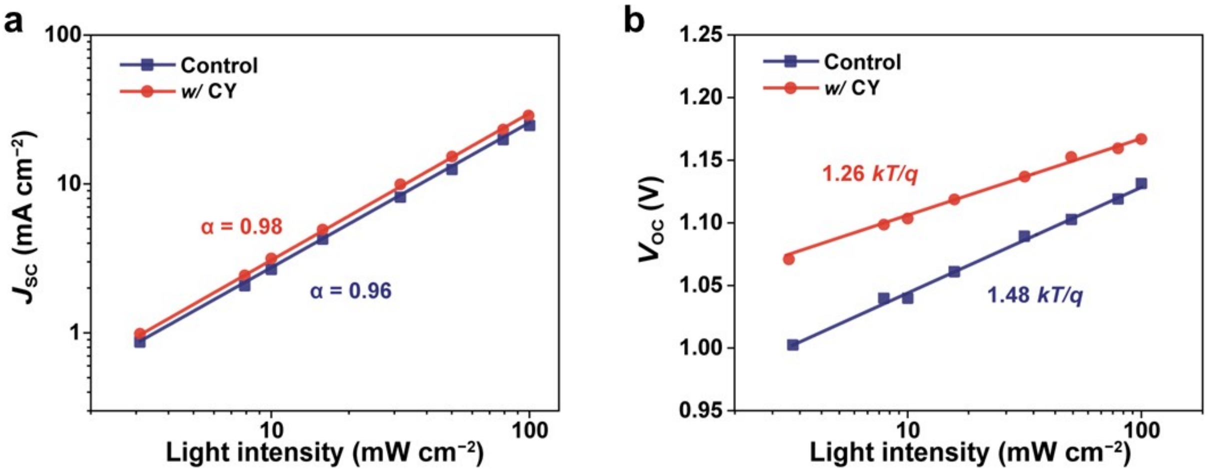

Figure S35. Light-intensity dependent (**a**) J_{sc} and (**b**) V_{oc} profiles of control and CY-incorporated PSCs.

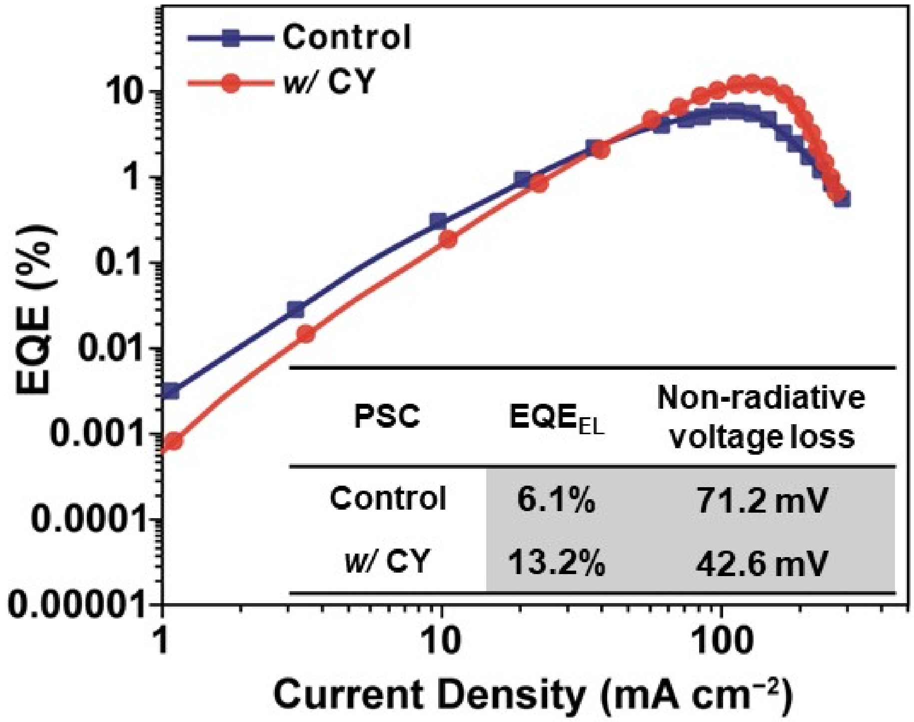

PSC	EQE_{EL}	Non-radiative voltage loss
Control	6.1%	71.2 mV
w/ CY	13.2%	42.6 mV

Figure S36. EQE_{EL} spectra of control and CY-incorporated PSCs.

Table S5. Fit parameters[a] for the time-resolved PL traces of control, CY-coated and CY-incorporated films taken at 770 ± 2 nm when excited at 510 nm.

Sample	I_1 (counts)	τ_1 (ns)	I_2 (counts)	τ_2 (ns)	I_3 (counts)	τ_3 (ns)	I_{tot} (counts)	$<\tau_{avg}>$[b]
Control	1136 (± 40)	7.2 (± 0.2)	44 (± 9)	46 (± 11)	8 (± 1)	662 (± 70)	1188 (± 41)	13 (± 1)
w/CY (surface-coated)	765 (± 47)	11.4 (± 1.3)	96 (± 58)	31 (± 11)	9 (± 1)	503 (± 42)	870 (± 75)	18 (± 3)
w/CY (incorporated)	960 (± 170)	3.1 (± 0.5)	1280 (± 14)	33 (± 1)	12 (± 1)	476 (± 14)	2252 (± 171)	22 (± 2)

[a] The time-resolved PL profiles were fitted to multi-exponential decay functions: $I(t) = \sum_n I_n e^{\{(t-t_0)/\tau_n\}}$. [b] Weight-averaged exciton lifetimes.

Table S6. Fit parameters[a] for the fs-TA kinetic profiles of control, CY-coated and CY-incorporated films taken at 756 ± 3 nm when excited at 505 nm.

Sample	ΔA_1 (mOD)	τ_1 (ps)	ΔA_2 (mOD)	τ_2 (ps)	ΔA_3 (mOD)	τ_3[b] (ns)
Control	–0.36 (± 0.01)	0.90 (± 0.05)	–0.57 (± 0.01)	697 (± 15)	–0.43 (± 0.01)	13
w/CY (surface-coated)	–0.36 (± 0.02)	0.48 (± 0.03)	–0.33 (± 0.01)	880 (± 31)	–0.67 (± 0.01)	18
w/CY (incorporated)	–0.35 (± 0.04)	0.35 (± 0.03)	–0.20 (± 0.00)	377 (± 15)	–0.79 (± 0.00)	22

[a] The TA kinetic profiles were fitted to multi-exponential decay functions: $\Delta A(t) = \sum_n \Delta A_n e^{\{(t-t_0)/\tau_n\}}$. [b] $<\tau_{avg}>$ in **Supplementary Table 5** were used to estimate the τ_3 components of the TA kinetic profiles due to the inaccuracy of the fits for components lasting longer than 3 ns, the maximum time window of our measurements.

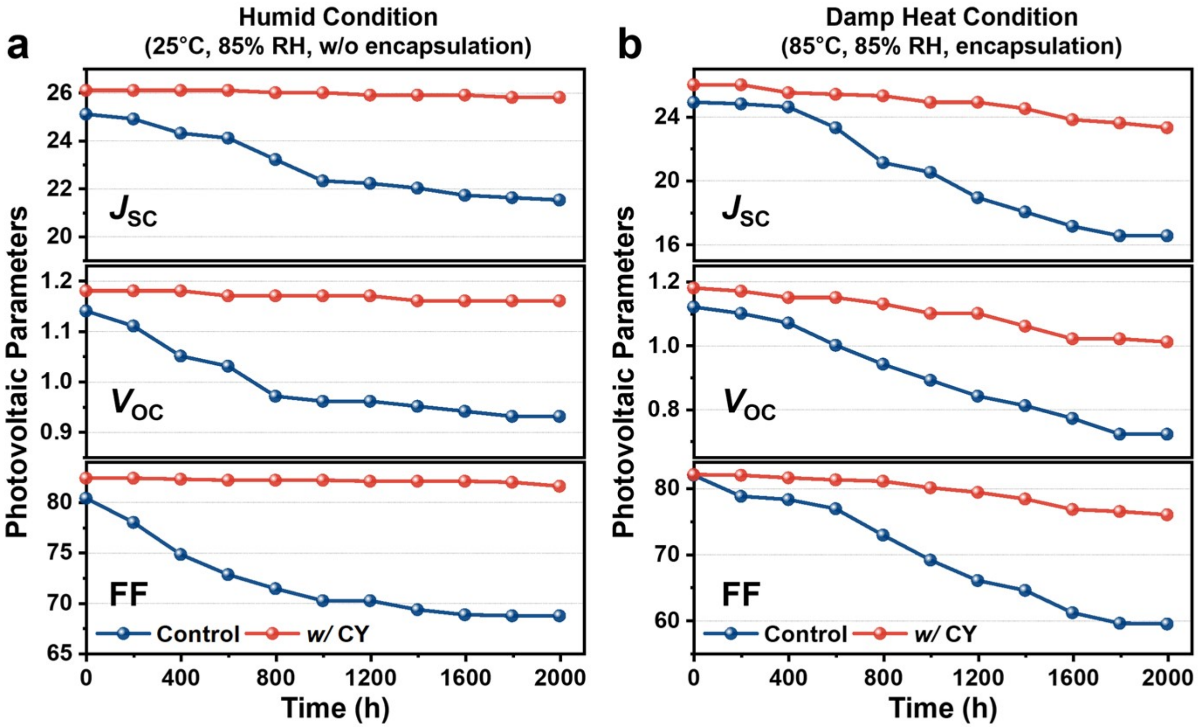

Figure S37. Change in photovoltaic parameters of the control and CY-incorporated PSCs over a period of 2000 h (A) under humid condition (85% RH, 25°C, w/o encapsulation) and (B) damp heat condition (85% RH, 85°C, encapsulation).

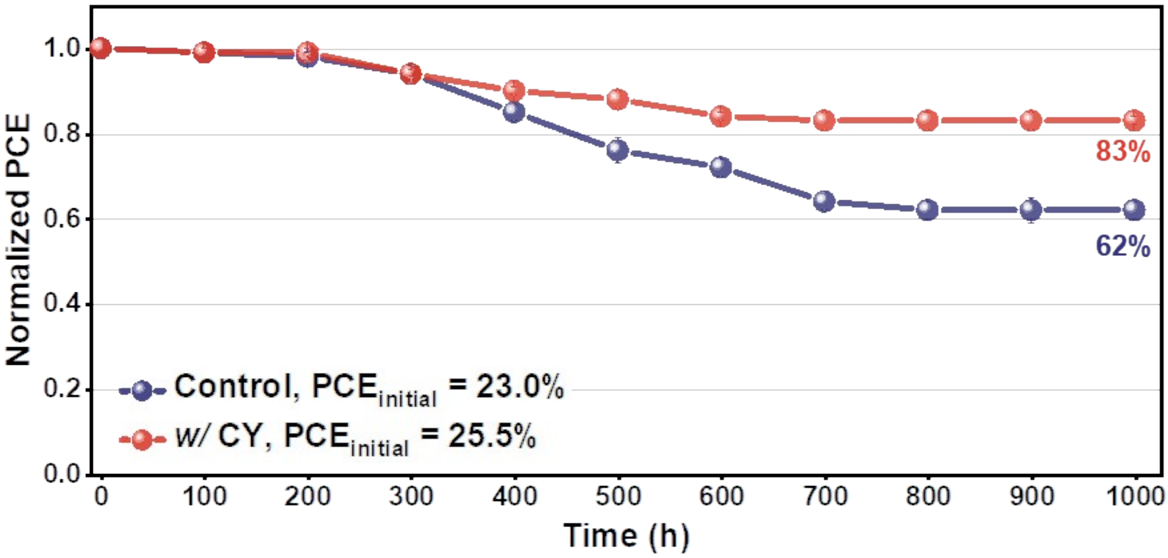

Figure S38. Normalized PCEs of the control and CY-incorporated PSCs after exposure to MPP conditions at 100-hour intervals without encapsulation.

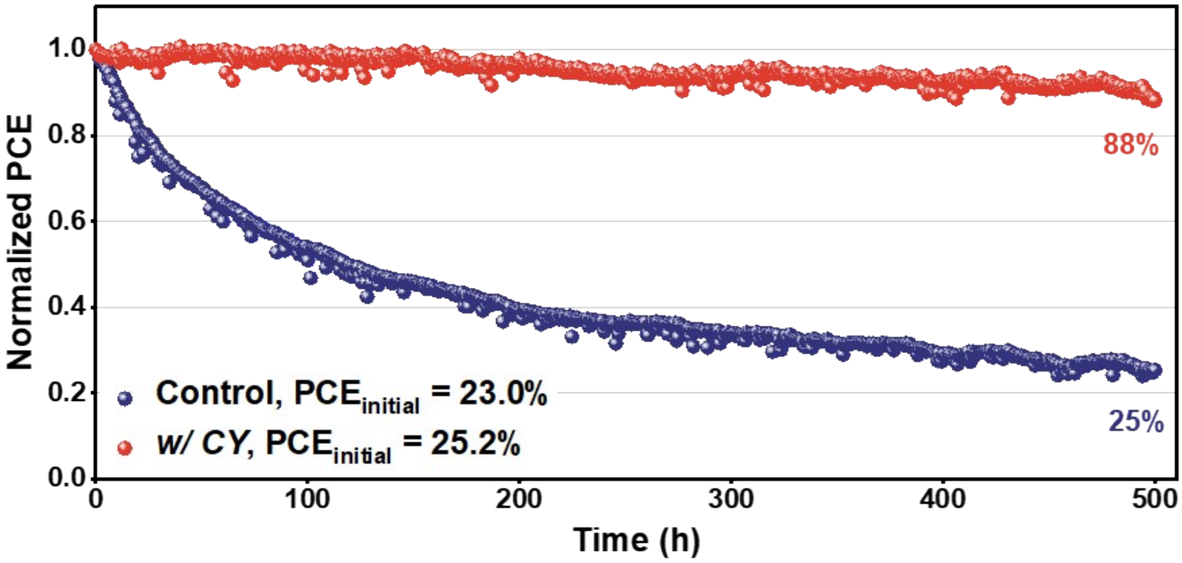

Figure S39. Normalized PCEs of the control and CY-incorporated PSCs under MPP tracking conditions at 25°C and 50% RH with encapsulation.

Table S7. Photovoltaic parameters of CY-incorporated PSCs with an area of 1 cm^2.

	Scan direction	V_{OC} [V]	J_{SC} [mA cm^{-2}]	FF [%]	PCE [%]
Large-area PSC	R	1.13	24.8	81.0	22.7
	F	1.09	24.2	78.6	20.7

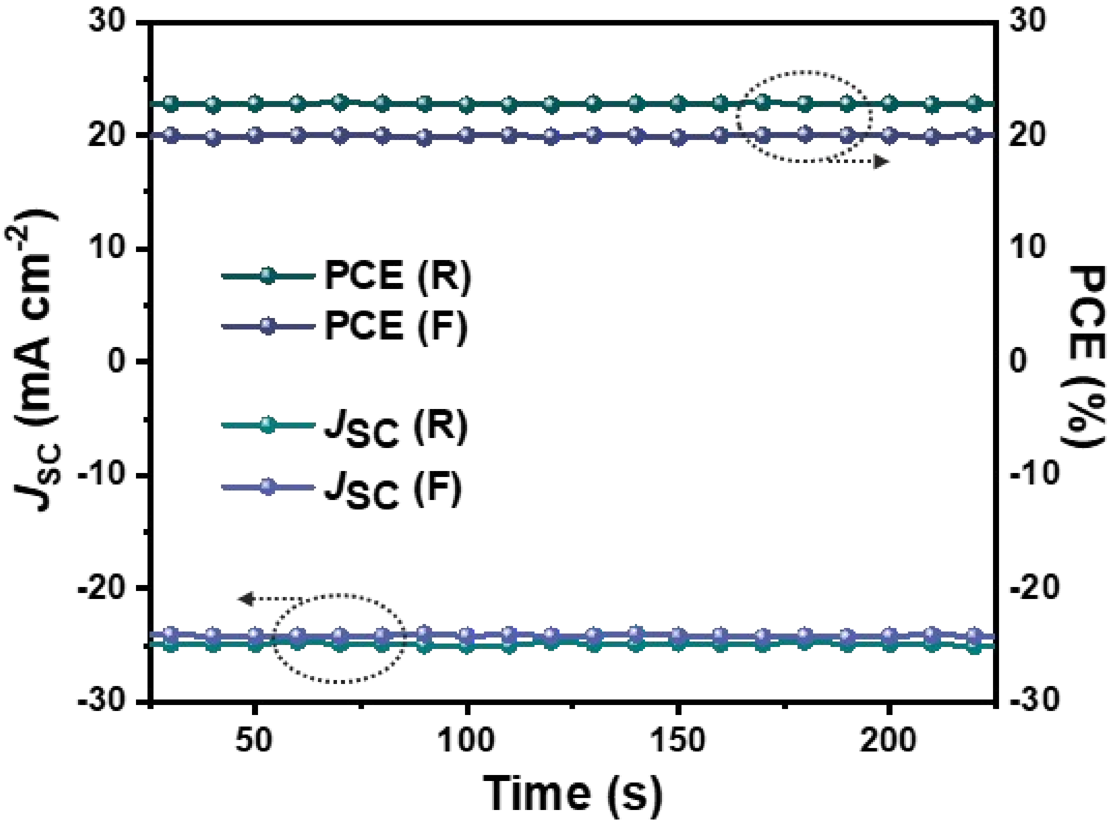

Figure S40. Steady-state photocurrent and PCE of large-area (1.0 cm^2) CY-incorporated PSC obtained by maximum power point tracking method.

Table S8. The summarized PCE and stability of the reported state-of-the-art additive-engineered PSCs from 2023 to 2025.

Date	Device structure	PCE (certified) (%)	Stability test conditions (PCE retention)	Additive	Ref
2023	FTO/CBD-$SnO_2/FA_{0.95}MA_{0.05}Pb(I_{0.95}Br_{0.05})_3$/FTPA/spiro-OMeTAD/Au	24.1	(1) AM 1.5G, N_2, 23°C, w/o encap. (95% for 1,000 h) (2) 50% RH, 23°C, w/o encap. (95% for 2,000 h) (3) 65°C, N_2, w/o encap. (85% for 500 h)	FTPA	4
2023	FTO/$ZnTiO_3$-ZnS/$TiO_2/FAPbI_3$/spiro-OMeTAD/Au	24.1	(1) 85% RH, 85°C, encap. (91% for 2,000 h) (2) AM 1.5G, 50% RH, 85°C, encap. (90% for 250 h)	NES	5
2023	ITO/$SnO_2/(FA_{0.95}MA_{0.05})_{0.95}Cs_{0.05}Pb(I_{0.95}Br_{0.05})_3$/Spiro-OMeTAD or PTAA/Au	24.2	(1) 30% RH, 85°C, N_2, w/o encap. (80% for >1,000 h) (2) AM 1.5G, 20% RH, 25°C, w/o encap. (97% for 1,000 h)	BMDP-TSA	6
2023	FTO/$SnO_2/FA_{0.90}MA_{0.03}Cs_{0.07}Pb(I_{0.92}Br_{0.08})_3$/PEAI/Spiro-OMeTAD/Au	23.2	(1) 30% RH, 25°C, w/o encap. (92% for 1,200 h) (2) 75% RH, 25°C, w/o encap. (89% for 720 h)	DLBA	7
2023	ITO/$SnO_2/MAPbI_3$/Spiro-OMeTAD/Ag	20.62	(1) 65% RH, w/o encap. (76% for 320 h) (2) AM 1.5G, 85% RH, w/o encap. (91% for 3 h)	TAA	8
2023	ITO/$SnO_2/FA_{0.85}Cs_{0.15}PbI_3$/Spiro-OMeTAD/Ag	22.42	25% RH, 25°C, w/o encap. (91% for 1,200 h)	5-ADI	9
2024	FTO/$SnO_2/FAPbI_3$/HABr/spiro-OMeTAD/Au	26.11 (25.8)	AM 1.5G, N_2, 55°C, w/o encap. (87.5% for 950 h)	METEAM	10
2024	ITO/$SnO_2/FAPbI_3$/Spiro-OMeTAD/Au	24.51	AM 1.5G, N_2, 25°C, w/o encap. (90.4% for 1,000 h)	PTAC	11
2024	FTO/$TiO_2/SnO_2/FA_{0.98}MA_{0.02}PbI_3$/Spiro-OMeTAD/Ag	24.15	(1) AM 1.5G, 35% RH, w/o encap. (91% for 1,200 s) (2) 40% RH, w/o encap. (88% for 120 h)	PhDMADBr	12
2024	FTO/$SnO_2/FA_{0.9}MA_{0.1}PbI_3$/Spiro-OMeTAD/Au	24.63	(1) 25% RH, 25°C, w/o encap. (91.52% for 2,160 h) (2) AM 1.5G, N_2, w/o encap. (93.13% for 1,200 h)	TMAC	13

2024	ITO/SnO_2/$FAPbI_3$/CHMAI/Spiro-OMeTAD/Au	26.12 (25.84)	(1) 25% RH, RT, w/o encap. (90% for 1,000 h) (2) 25% RH, 85°C, w/o encap. (54.7% for 500 h)	BAAc	14
2024	ITO/SnO2/$FA_{0.93}MA_{0.07}PbI_3$/Spiro-OMeTAD/Ag	25.32	(1) N_2, RT, w/o encap. (94% for 70 days) (2) AM 1.5G, N_2, encap. (95% for 1,200 h) (3) 45% RH, RT, w/o encap. (92% for 480 h) (4) 85°C, w/o encap. (90% for 360 h)	6BAS	15
2024	FTO/TiO_2/$FAPbI_3$/Spiro-OMeTAD/Au	25.28	RH = 25%, 25°C, w/o encap. (95.74% for 1,152 h)	DFA	16
2024	FTO/SnO_2/$(FAPbI_3)_{0.99}(MAPbBr_3)_{0.01}$/Spiro-OMeTAD/Au	23.05	(1) AM 1.5G, 25% RH, w/o encap. (75% for 120 h) (2) 25% RH, w/o encap. (95% for 400 h)	4Me-BQ	17
2025	FTO/SnO_2/$FA_{0.93}MA_{0.07}PbI_3$/Spiro-OMeTAD/Au	25.27 (25.04)	(1) AM 1.5G, N_2, w/o encap. (80% for 2,500 h) (2) N_2, 65°C, w/o encap. (81% for 700 h) (3) 20% RH, 20°C, w/o encap. (82% for 2,200 h)	BNCl	18
2025	FTO/bl-SnO_x/SnO_2/$FAPbI_3$/Spiro-OMeTAD/Au	25.21 (23.51)	AM 1.5G, 25% RH, 60°C, encap. (91.68% for 1,080 h)	DEACl, Fo	19
2025	ITO/SnO_2/$FA_{0.95}Cs_{0.05}PbI_3$/spiro-OMeTAD/Ag	26.15 (25.59)	(1) 85% RH, 85°C, encap. (90.6% for 500 h) (2) AM 1.5G, 65°C, N_2, encap. (90.3% for 500 h)	SBMA, HEA	20
2025	FTO/SnO_2/$FAPbI_3$/4-MeO-PEAI/Spiro-OMeTAD or PTAA/Ag or Au	24.5	(1) 90% RH, 25°C, w/o encap. (90% for 3,216 h) (2) AM 1.5G, N_2, w/o encap. (96% for 2,616 h) (3) 25% RH, 23°C, w/o encap. (95% for 8,000 h)	PyCl, AchCl, FAAc	21
2025	ITO/SnO_2/$FAPbI_3$/Spiro-OMeTAD/Ag	23.21	(1) 50% RH, RT, w/o encap. (89% for 1,000 h) (2) 35% RH, 65°C, w/o encap. (87% for 1,000 h)	4FPA	22
2025	FTO/TiO_2/SnO_2/$Cs_{0.05}FA_{0.90}MA_{0.05}PbI_3$/Spiro-OMeTAD/Au	24.8	(1) 35% RH, 25°C, w/o encap. (89% for 864 h) (2) N_2, 65°C w/o encap. (79% for 648 h)	SacS	23
2025	FTO/TiO_2/$FAPbI_3$/Spiro-OMeTAD/Au	26.0 (25.28)	(1) 85% RH, 25°C, w/o encap. (96% for 2,000 h) (2) AM 1.5G, N_2, w/o encap. (83% for 1,000 h) (3) AM 1.5G, 50% RH, 25°C, encap. (88% for 500 h) (4) 85% RH, 85°C, encap. (71% for 1,000 h)	**CY**	**This Work**

Reference

1. J. Yuan, Y. Zhang, L. Zhou, G. Zhang, H.-L. Yip, T.-K. Lau, X. Lu, C. Zhu, H. Peng, P. A. Johnson, M. Leclerc, Y. Cao, J. Ulanski, Y. Li and Y. Zou, *Joule*, 2019, **3**, 1140-1151.
2. W. L. Kalb and B. Batlogg, *Phys. Rev. B*, 2010, **81**, 035327.
3. S. M. Menke, N. A. Ran, G. C. Bazan and R. H. Friend, *Joule*, 2018, **2**, 25-35.
4. M. Li, R. Sun, J. Chang, J. Dong, Q. Tian, H. Wang, Z. Li, P. Yang, H. Shi, C. Yang, Z. Wu, R. Li, Y. Yang, A. Wang, S. Zhang, F. Wang, W. Huang and T. Qin, *Nat Commun*, 2023, **14**, 573.
5. X. Huang, F. Cao, S. Zhan, Q. Feng, M. Zhu, Z. Su, X. Gao, J. Yin, J. Li, N. Zheng and B. Wu, *Joule*, 2023, **7**, 1556-1573.
6. H. Wen, Z. Zhang, Y. Guo, W. Luo, S. Si, T. Yin, H. Wu and S. Huang, *Advanced Energy Materials*, 2023, **13**.
7. X. Jiang, B. Zhang, G. Yang, Z. Zhou, X. Guo, F. Zhang, S. Yu, S. Liu and S. Pang, *Angew Chem Int Ed Engl*, 2023, **62**, e202302462.
8. W. Zhang, M. Yuan, L. Han, G. Luo, L. Zhang, H. He, P. Lin, L. Xu, X. Wu, X. Zhu, X. Yu, P. Wang and C. Cui, *ACS Applied Energy Materials*, 2023, **6**, 7003-7013.
9. K. Wang, B. Yu, C. Lin, R. Yao, H. Yu and H. Wang, *Solar RRL*, 2023, **7**.
10. X. Li, S. Gao, X. Wu, Q. Liu, L. Zhu, C. Wang, Y. Wang, Z. Liu, W. Chen, X. Li, P. Xiao, Q. Huang, T. Chen, Z. Li, X. Gao, Z. Xiao, Y. Lu, X. Zeng, S. Xiao, Z. Zhu and S. Yang, *Joule*, 2024, **8**, 3169-3185.
11. H. Wang, Z. Zhang, X. Wang, L. Duan and J. Luo, *Nano Energy*, 2024, **123**.
12. X. Zhang, X. Wang, Y. Yin, Y. Zhang, L. Liu, Q. Li, L. Duan, X. Ban and L. Shi, *Chemical Engineering Journal*, 2024, **495**.
13. X. Wang, S. Liu, H. Wang and J. Luo, *Advanced Functional Materials*, 2024, **34**.
14. Q. Zhang, C. Zhao, J. Xu, F. Shen, Y. Wang, B. Ji, X. Guan, S. Ma, Y. Wu, Z. Li and J. Yao, *Advanced Functional Materials*, 2025, DOI: 10.1002/adfm.202507934.

15. T. Wu, P. Wang, L. Zheng, Y. Zhao and Y. Hua, *Advanced Energy Materials*, 2024, **14**.
16. Y. Cao, N. Yan, M. Wang, D. Qi, J. Zhang, X. Chen, R. Qin, F. Xiao, G. Zhao, Y. Liu, X. Cai, K. Zhao, S. F. Liu and J. Feng, *Angew Chem Int Ed Engl*, 2024, **63**, e202404401.
17. D.-N. Lee, Y.-S. Jeon, S. C. Cho, S. U. Lee and N.-G. Park, *ACS Energy Letters*, 2024, **9**, 4172-4179.
18. J. Zhou, J. Lv, L. Tan, H. Li, B. Jiao, M. Li, Y. Liu, C. Jiang, R. Hua and C. Yi, *Adv Mater*, 2025, DOI: 10.1002/adma.202502916, e2502916.
19. X. Lin, H. Su, X. Shen, Z. Qin, M. Chen, Z. Zhang, G. Zheng, Y. Wang and L. Han, *Adv Mater*, 2025, DOI: 10.1002/adma.202418008, e2418008.
20. C. Shao, J. Ma, G. Niu, Z. Nie, Y. Zhao, F. Wang and J. Wang, *Adv Mater*, 2025, **37**, e2417150.
21. Z. Xiong, Y. S. Jeon, H. Wang, G. Fu, S. H. Cho, S. J. Chang, P. A. van Aken and N. G. Park, *Adv Mater*, 2025, **37**, e2413712.
22. T. Dong, J. Liao, H. Li, J. Li, H. Li, Z. Li, L. Tan, X. Chen and W. Zhang, *ACS Appl Mater Interfaces*, 2025, **17**, 12291-12298.
23. Z. Yang, A. Sun, Y. Ren, Z. Li, L. Mo, H. Zhang, Y. Huang and L. Hu, *Small*, 2025, DOI: 10.1002/smll.202503279, e2503279.